Efficient Estimation of Cardiac Conductivities: a Proper Generalized Decomposition Approach

Alessandro Barone, Michele Giuliano Carlino, Alessio Gizzi, Simona Perotto, Alessandro Veneziani

Efficient Estimation of Cardiac Conductivities: a Proper Generalized Decomposition Approach

Alessandro Barone[a,*], Michele Giuliano Carlino[b,c], Alessio Gizzi[d], Simona Perotto[e], Alessandro Veneziani[a,f]

[a]*Department of Mathematics, Emory University, Atlanta (GA), USA*
[b]*INRIA, Bordeaux, FRANCE*
[c]*IMB, Université de Bordeaux, FRANCE*
[d]*Department of Engineering, Campus Bio-Medico University of Rome, Via A. del Portillo 21, 00128 Rome, ITALY*
[e]*MOX, Dipartimento di Matematica, Politecnico di Milano, ITALY*
[f]*Department of Computer Science, Emory University, Atlanta, GA, USA*

Abstract

While the potential groundbreaking role of mathematical modeling in electrophysiology has been demonstrated for therapies like cardiac resynchronization or catheter ablation, its extensive use in clinics is prevented by the need of an accurate customized conductivity identification. Data assimilation techniques are, in general, used to identify parameters that cannot be measured directly, especially in patient-specific settings. Yet, they may be computationally demanding. This conflicts with the clinical timelines and volumes of patients to analyze. In this paper, we adopt a model reduction technique, developed by F. Chinesta and his collaborators in the last 15 years, called Proper Generalized Decomposition (PGD), to accelerate the estimation of the cardiac conductivities required in the modeling of the cardiac electrical dynamics. Specifically, we resort to the Monodomain Inverse Conductivity Problem (MICP) deeply investigated in the literature in the last five years. We provide a significant proof of concept that PGD is a breakthrough in solving the MICP within reasonable timelines. As PGD relies on the offline/online paradigm and does not need any preliminary knowledge of the high-fidelity solution, we show that the PGD online phase estimates the conductivities in real-time for both two-dimensional and three-dimensional cases, including a patient-specific ventricle.

Keywords: Computational Electrophysiology, Model Order Reduction, Data Assimilation, Proper Generalized Decomposition, Parameter Identification

1. Introduction

The use of mathematical computational models in medicine is a consolidated approach (sometimes called *in silico* working, alongside the traditional *in vivo* and *in vitro* analyses) to have a deep understanding of physio-pathological dynamics. However, the complete translation of these models to clinical practice

*Department of Mathematics, Emory University, Atlanta (GA), USA, e-mail: alebarone23@gmail.com

is prevented by several factors, including the need for their accurate customization to reflect the specific patient's condition [1]. This requires accurate image processing procedures for the morphology retrieval as well as the personalized identification of model parameters. The parameters often cannot be measured and their fine tuning can be obtained only after data assimilation procedures (see, e.g., [2, 3, 4, 5]), i.e., specific methodologies to combine available measures and numerical solutions for an enhanced modeling. Different approaches can be used to include a measurable quantity into the mathematical modeling process. In sequential stochastic procedures, the parameters are included as unknowns (or state variables) of the problem and are subject to an estimation procedure generally aimed to minimize the variance of the estimate or to maximize a probability density function. In variational approaches, the parameters to identify are used as control variables in the minimization of the mismatch between the results of the numerical model and the observed dynamics. In this way, the knowledge of observable quantities is converted into an estimate of the non-observable ones.

Data assimilation strategies [6, 7] are generally very powerful and able of an accurate personalization. However, they have intrinsic limitations and, in general, they may entail significant computational costs. Thus, as clinical problems often require relatively short timelines, empirical approaches are generally preferred to privilege efficiency over accuracy. In this way, the core knowledge of physiological and pathological dynamics expressed by physic-based models is discarded. This may be detrimental for patients whose features do not fall into the set of data used for the empirical methods.

In order to improve the efficiency of rigorous identification procedures, model reduction techniques can be used to replace high-fidelity models with educated surrogates, yet including the core knowledge of the problem at hand. Model reduction is an important topic developed over the years in the engineering and mathematical literature as the increased computational power was not able to cover the even more progressively rising complexity of problems addressed by mathematical modeling (see, e.g., [8, 9, 10, 11, 12, 13]). Life sciences and medicine certainly fall in this picture.

In this work, we address a data assimilation problem of cardiac electrophysiology. The knowledge of the differential equations for the potential propagation in the cardiac tissue is quite consolidated, as witnessed by the specific literature (see, e.g., [14, 15, 16]). Modeling improvements are mainly devoted to the micro-, meso- and macroscopic (i.e., cell, tissue and organ levels) description of the ions dynamics at cellular and subcellular level [17], to their behavior at the cell-cell interface [18, 19], and to the spatio-temporal coupling among the different cardiac components resulting in synchronized emerging phenomena [20]. These models feature parameters that are quite hard to measure *in vivo* and data assimilation procedures have been recognized as a viable approach [21, 22]. In particular, variational techniques for the estimation of the tensor of the cardiac conductivities of the classical Bidomain and Monodomain models have been addressed and

analyzed in [23]. The reliability of this approach for solving the Bidomain/Monodomain Inverse Conductivity Problem has been demonstrated on several benchmarks, covering synthetic as well as *in vitro* cases [24, 25]. However, the efficiency of such procedures needs to be properly addressed, as the computational cost of the iterative mismatch minimization is generally high, especially when dealing with real geometries. This problem has been promptly recognized as a bottleneck, and several *Reduced-Order Models* (ROMs) have been investigated [26, 27, 28, 29, 13]. The proposed approaches rely on the construction of a surrogate, as a combination of basis functions generally built moving from previous solutions (called "snapshots") for a predetermined set of values for the parameters. For instance, in the Proper Orthogonal Decomposition (POD) considered in [29], the snapshots are smartly selected based on the concept of domain of influence in the space of the conductivities, and the surrogate is constructed after a Singular Value Decomposition (SVD) of the snapshot matrix.

In this paper, we explore a ROM procedure that does not require any *a priori* knowledge of the solution, even though it still relies on an offline/online paradigm. The Proper Generalized Decomposition (PGD) is a model reduction technique introduced by F. Chinesta et al. [30], specifically devised to efficiently evaluate a parametrized differential problem when varying the parameter values. The idea is to treat the problem parameters as additional independent variables and to compute the solution over an extended domain, inclusive of the range the parameters are expected to belong to. As the actual numerical computation is performed in a highly dimensional domain during the offline stage, a special representation is introduced, where the surrogate solution is factorized with respect to each independent variable (including the parameters) or low-dimensional groups of variables. By advocating an iterative approach to compute this factorization, PGD proved to be an effective technique to reliably approximate several parametric problems [31, 32, 33]. Actually, in the online phase, the solution is ready to be promptly evaluated for any value of the parameters as well as of the independent variables. This is particularly effective in a variational parameter identification procedure, when the solution for different guesses of the parameter(s) is tested in an iterative minimization process.

Based on these general properties, in this paper we explore the use of PGD to solve the Monodomain Inverse Conductivity Problem (MICP). After a short introduction to PGD in Section 2, we present the Monodomain model, the MICP and its basic features in Section 3. Successively, we introduce the specific technical aspects of the application of PGD to the Monodomain problem in Section 4. We detail the PGD approximation to the Monodomain problem in Section 4.1 and address implementation details in Section 4.2. In Section 4.3 we assess the accuracy of the PGD model over a number of test cases. We start with a two-dimensional (2D) test problem, yet in a morphology based on a previous study on canine tissues. Then, we extend the procedure to three-dimensional (3D) problems, including a patient-specific left ventricle. Finally,

we apply PGD to the solution of MICP in Section 5. All the results pinpoint that, in spite of an offline stage that may be quite demanding in terms of CPU time, the PGD dramatically reduces the parameter identification to nearly real-time computations on common computational architectures. These preliminary results encourage further work for the extension of the methodology to the clinical practice (Section 6).

2. The PGD in a Nutshell

For the sake of completeness, we provide a short introduction to the PGD, to recall the basic ideas and provide some notation and terminology. For a more complete introduction, the reader is referred to [30, 34, 35].

In what follows, $\Omega \subset \mathbb{R}^d$ is the physical space domain, with $d = 2, 3$. We denote by V a Hilbert space, generally a subspace of the Sobolev space $H^1(\Omega)$ [36]. With $\boldsymbol{q} \in \mathbf{R}^\delta$ we denote a vector of parameters the problem we consider depends on. Let us focus on a generic parametrized elliptic problem in the weak form: find $u \in V$ s.t.

$$a_{\boldsymbol{q}}(u, v) = F_{\boldsymbol{q}}(v) \quad \forall v \in V, \tag{1}$$

where, for any given admissible value of the parameters in $\boldsymbol{q}$, $a_{\boldsymbol{q}} : V \times V \to \mathbb{R}$ and $F_{\boldsymbol{q}} : V \to \mathbb{R}$ are a bilinear, continuous and coercive and a linear continuous form, respectively. More precisely, we assume that the parameter q_i, for $i = 1, \dots \delta$, ranges in an admissible interval $\mathcal{S}_i$, so that the admissible set for $\boldsymbol{q}$ is the cuboid $\boldsymbol{\mathcal{S}} \equiv \mathcal{S}_1 \times \mathcal{S}_2 \dots \times \mathcal{S}_\delta$. According to a PGD procedure, we regard the solution u as a function of $\boldsymbol{x} \in \mathbb{R}^d$ and $\boldsymbol{q} \in \mathbb{R}^\delta$. Specifically, we assume that $u \in W = V \otimes \bigotimes_{l=1}^{\delta} L^2(\mathcal{S}_l)$. Thus, the *extended* weak formulation, including the parameters as independent variables, is obtained by integrating (1) over $\boldsymbol{\mathcal{S}}$ and coincides with the $(d + \delta)$-dimensional problem: find $u \in W$ s.t.

$$\mathcal{A}(u, v) = \mathcal{F}(v), \qquad \forall v \in W, \tag{2}$$

with $\mathcal{A} : W \times W \to \mathbb{R}$ and $\mathcal{F} : W \to \mathbb{R}$ given by

$$\mathcal{A}(u, v) \equiv \int_{\boldsymbol{\mathcal{S}}} a_{\boldsymbol{q}}(u, v) d\boldsymbol{q}, \quad \mathcal{F}(v) \equiv \int_{\boldsymbol{\mathcal{S}}} F_{\boldsymbol{q}}(v) d\boldsymbol{q}, \tag{3}$$

respectively. With a little abuse of notation, we keep denoting the unknown and the test functions with the same symbols, u, v, although their dependence on the parameters in $\boldsymbol{q}$.

As the dimension of the problem is now increased, the numerical solution (e.g., with a generic Galerkin approach) may be problematic. We therefore proceed under the assumption of *separability*, that is typi-

cally postulated for unsteady problems to separate the space to the time dependence of the solution (semi-discretization). This means that the reduced solution is regarded as the linear combination of factors breaking up the dependence on the different independent variables into the product of low-dimensional separated functions. Consequently, the PGD approximation of the problem takes the form

$$u_m(\boldsymbol{x};\boldsymbol{q}) = \sum_{k=1}^{m} u_k^{\boldsymbol{x}}(\boldsymbol{x}) \prod_{l=1}^{\delta} u_k^l(q_l), \tag{4}$$

for $m \in \mathbb{N}^+$, where functions $u_k^{\boldsymbol{x}} \in V_h \subset V$ account for the $\boldsymbol{x}$-dependence of the solution, while functions $u_k^l \in Q^l \subset L^2(\mathcal{S}_l)$, for $l = 1, 2, \dots \delta$, carry the dependence on the parameters, V_h and Q^l being discrete spaces with $\dim(V_h) = N_h^{\boldsymbol{x}}$ and $\dim(Q^l) = N^l$, respectively. The separability assumption is applied also to the extended bilinear and linear forms in (2), so that we have

$$\mathcal{A}(u,v) = \sum_{\alpha=1}^{N_a} a_\alpha^{\boldsymbol{x}}(u_\psi^{\boldsymbol{x}}, v_\beta^{\boldsymbol{x}}) \prod_{l=1}^{\delta} a_\alpha^l(u_\psi^l, v_\beta^l), \quad \mathcal{F}(v) = \sum_{\varphi=1}^{N_F} F_\varphi^{\boldsymbol{x}}(v_\beta^{\boldsymbol{x}}) \prod_{l=1}^{\delta} F_\varphi^l(v_\beta^l), \tag{5}$$

with $a_\alpha^{\boldsymbol{x}} : V \times V \to \mathbb{R}$ and $a_\alpha^l : L^2(\mathcal{S}_l) \times L^2(\mathcal{S}_l) \to \mathbb{R}$ bilinear forms, for $\alpha = 1, \dots, N_a$, $F_\varphi^{\boldsymbol{x}} : V \to \mathbb{R}$ and $F_\varphi^l : L^2(\mathcal{S}_l) \to \mathbb{R}$, linear forms, for $\varphi = 1, \dots, N_F$, where N_a, $N_F \in \mathbb{N}^+$ and indices ψ, $\beta = 1, \dots, m$ strictly depend on the differential operators involved in the definition of $\mathcal{A}$ and $\mathcal{F}$, the test function v being rewritten in a separate form as well [30].

Now, we define the space of the functions in (4), i.e. the PGD space,

$$W_m = \left\{ w_m(\boldsymbol{x};\boldsymbol{q}) = \sum_{k=1}^{m} w_k^{\boldsymbol{x}}(\boldsymbol{x}) \prod_{l=1}^{\delta} w_k^l(q_l), \text{ with } w_k^{\boldsymbol{x}} \in V_h,\, w_k^l \in Q^l, l = 1, \dots, \delta,\, \boldsymbol{x} \in \Omega,\, \boldsymbol{q} \in \boldsymbol{\mathcal{S}} \right\}. \tag{6}$$

Differently from a standard Galerkin approach, the separated functions, $u_k^{\boldsymbol{x}}$, u_k^l in (4), are not selected a-priori (e.g., as piecewise or Gaussian polynomials). Conversely, the computation of these functions is the result of a progressive construction customized on the problem to solve, performed in an iterative way that takes advantage of the factorization in (4). In more details, the computation of u_m is based on two steps: (i) a "greedy" weighted residual step to *enrich* the approximation $u_{m-1} \in W_{m-1}$ to $u_m \in W_m$, by adding the new contribution (or *mode*) $\delta_m u \equiv u_m^{\boldsymbol{x}}(\boldsymbol{x}) \prod_{l=1}^{\delta} u_m^l(q_l)$; (ii) a factorized computation of the m-th term, $\delta_m u$, based on a fixed-point iteration method called *Alternating-Direction Strategy* (ADS) [30, 34, 35].

As for (i), we aim to find the new mode, $\delta_m u$, by solving the weighted residual problem

$$\mathcal{A}(u_{m-1} + \delta_m u, v_m) = \mathcal{F}(v_m), \qquad \forall v_m \in W_m, \tag{7}$$

where $u_{m-1} \in W_{m-1}$ is the available approximation (for $m = 1$, typically, one sets $u_0 = 0$). The progressive addition of new terms stops when the PGD solution no longer changes significantly. Technically, this leads to the (external) convergence criterion

$$\frac{\|u_m\|}{\|u_1\|} \leq \text{tol}_e, \tag{8}$$

where the tolerance tol_e is user-defined and the norm can be selected in different ways (e.g., in $H^1(\Omega) \otimes \bigotimes_{l=1}^{\delta} L^2(\mathcal{S}_l)$). The rationale is that the new modes add a progressively less relevant information to the solution (as it happens, for instance, with a Sturm-Liouville Eigenvalue expansion [37]), so that the left-hand side of (8) does actually reduce when m increases.

As for (ii), we perform the computation of $\delta_m u$ in (7) by solving iteratively the component dependence on each variable (or set of variables) independently, in an alternating direction framework. Introducing the fixed-point iterative index, $j \geq 1$, let us assume to have a guess $\delta_{m,j-1}u(\boldsymbol{x};\boldsymbol{q}) = u^{\boldsymbol{x}}_{m,j-1}(\boldsymbol{x}) \prod_{l=1}^{\delta} u^l_{m,j-1}(q_l)$ for $\delta_m u$ (for $j = 1$, $\delta_{m,0}u(\boldsymbol{x};\boldsymbol{q})$ is chosen according to the boundary conditions of the problem at hand). We start computing the contribution $u^{\boldsymbol{x}}_{m,j}$ by solving the d-dimensional problem

$$\mathcal{A}(u^{\boldsymbol{x}}_{m,j} \prod_{l=1}^{\delta} u^l_{m,j-1}, v_m) = \mathcal{F}(v_m) - \mathcal{A}(u_{m-1}, v_m), \tag{9}$$

where $v_m(\boldsymbol{x};\boldsymbol{q}) = v^{\boldsymbol{x}}_m(\boldsymbol{x}) \prod_{l=1}^{\delta} u^l_{m,j-1}(q_l)$, for any $v^{\boldsymbol{x}}_m \in V_h$. Successively, we tackle the dependence on the parameter q_r, for $r = 1, \ldots, \delta$, by solving the 1D problem

$$\mathcal{A}(u^{\boldsymbol{x}}_{m,j} u^r_{m,j} \prod_{l=1}^{r-1} u^l_{m,j} \prod_{l=r+1}^{\delta} u^l_{m,j-1}, v_m) = \mathcal{F}(v_m) - \mathcal{A}(u_{m-1}, v_m), \tag{10}$$

where $u^r_{m,j}$ is the unknown and we choose now $v_m(\boldsymbol{x};\boldsymbol{q}) = u^{\boldsymbol{x}}_{m,j}(\boldsymbol{x}) v^r_m(q_r) \prod_{l=1}^{r-1} u^l_{m,j}(q_l) \prod_{l=r+1}^{\delta} u^l_{m,j-1}(q_l)$, for any $v^r_m \in Q^r$. By solving (10) for $r = 1, \ldots, \delta$, we complete the computation of $\delta_m u$ in (7), by setting $\delta_m u(\boldsymbol{x};\boldsymbol{q}) = u^{\boldsymbol{x}}_m(\boldsymbol{x}) \prod_{l=1}^{\delta} u^l_m(q_l)$, with $u^{\boldsymbol{x}}_m(\boldsymbol{x}) = u^{\boldsymbol{x}}_{m,\tilde{j}}(\boldsymbol{x})$, $u^l_m(q_l) = u^l_{m,\tilde{j}}(q_l)$, $\tilde{j}$ denoting the fixed-point iteration index ensuring the convergence to problems (9)-(10). A standard stopping criterion for the (internal) iterative loops in (9) and (10) reads

$$\frac{\|\delta_{m,j}u - \delta_{m,j-1}u\|}{\|\delta_{m,j-1}u\|} \leq \text{tol}_i, \tag{11}$$

with tol_i a user-defined tolerance and $\delta_{m,\tau}u(\boldsymbol{x};\boldsymbol{q}) = u^{\boldsymbol{x}}_{m,\tau}(\boldsymbol{x}) \prod_{l=1}^{\delta} u^l_{m,\tau}(q_l)$, with $\tau = j-1$, j. Once this criterion is fulfilled, the PGD approximation $u_m(\boldsymbol{x};\boldsymbol{q}) = u_{m-1}(\boldsymbol{x};\boldsymbol{q}) + \delta_m u(\boldsymbol{x};\boldsymbol{q})$ is available. All the steps involved in (9)-(10) can be written in an algebraic form that we skip here for the sake of brevity (see, e.g., [38] for the explicit computations).

Algorithm 1 PGD algorithm (Offline phase)

Input: u_0, $\boldsymbol{\mathcal{S}}$, tol_e, tol_i, m_{max}, j_{max}
Set: $m \leftarrow 0$;
while $(\|u_m\|/\|u_1\| \leq \text{tol}_e \ \& \ m \leq m_{max})$ **do**
    Set: $m \leftarrow m + 1$;
    Set: $j \leftarrow 0$;
    Set $\delta_{m,0}u$;
    while $(\|\delta_{m,j}u - \delta_{m,j-1}u\|/\|\delta_{m,j-1}u\| \leq \text{tol}_i \ \& \ j \leq j_{max})$ **do**
        $j \leftarrow j + 1$;
        Solve (9);
        for $r = 1, \ldots, \delta$ **do**
            Solve (10);
        end for
    end while
    Set: $u_m^{\boldsymbol{x}}(\boldsymbol{x}) \leftarrow u_{m,j}^{\boldsymbol{x}}(\boldsymbol{x})$;
    Set: $u_m^r(q_r) \leftarrow u_{m,j}^r(q_r)$;
    Set: $u_m(\boldsymbol{x};\boldsymbol{q}) \leftarrow u_{m-1}(\boldsymbol{x};\boldsymbol{q}) + u_m^{\boldsymbol{x}}(\boldsymbol{x}) \prod_{r=1}^{\delta} u_m^r(q_r)$;
end while

The PGD procedure is summarized in Algorithm 1. Implementation details related specifically to the monodomain problem are deferred to Section 4.2. In particular, among the input parameters, m_{max} and j_{max} introduce an upper bound to the maximum number of enrichment and fixed-point iterations, respectively. Algorithm 1 is the so-called *offline* phase of the PGD method. After this phase, the reduced solution is available for any value of the independent variables, including the admissible set $\boldsymbol{\mathcal{S}}$ of the parameters. Thus, the cost of the online phase reduces to the cost of assembling the solution $u_m(\boldsymbol{x};\boldsymbol{q}) = \sum_{k=1}^{m} u_k^{\boldsymbol{x}}(\boldsymbol{x}) \prod_{l=1}^{\delta} u_k^l(q_l)$. This is a strategic property in view of a data assimilation procedure, where we need to iteratively estimate the solution of the problem of interest for different values of the parameters, to minimize the mismatch from the observations. At this time, we do not have theoretical results on the convergence of the loops involved in the offline phase. Actually, the ultimate goal of this work is assessing the reliability of the PGD model reduction, and verifying its computational competitiveness when solving the cardiac conductivities estimation problem.

3. The Monodomain Model

3.1. The Forward Problem

Propagation of the electrical signal in the cardiac tissue is the result of complex multiscale dynamics occurring over the whole heart, yet based on cellular kinetics. Well-established experimental evidences, originating from Hodgkin-Huxley famous studies, supported the description of the kinetics of ionic currents by means of local nonlinear reaction terms within a reaction-diffusion model [39]. These reaction functions require constitutive laws generally denoted by *ionic models*. They consist of a set of ordinary differential

equations capturing the dynamics of the ionic currents flowing throughout the cell membrane (generalization including intra-cellular reaction-diffusion processes, involving, e.g., Ca^{2+} ions, are also present in the literature [40]). In particular, they describe the time evolution of the so-called *gating variables*, which control the ionic fluxes and ensure the fulfillment of ion balance laws over the whole cell.

The mathematical modeling of the electrical activity of the heart has been the subject of many works. One of the most popular descriptions is the Bidomain model [16, 41]. This stems from a homogenized description of both the intra- and the extra-cellular potentials, that are defined on the same spatial domain, dropping a fine microscopic description of the intra- and extra-cellular regions. The model has been demonstrated to be accurate and reliable (specifically for defibrillation applications [42]), yet its degenerate nature of parabolic partial differential equation system (where the matrix multiplying the vector of time derivatives is actually singular) makes the efficient numerical solution quite challenging. This has justified an abundant literature on the efficient solution of the Bidomain model, in terms of algorithms, preconditioners and high-performance computing implementations (see, e.g., [43, 44, 45, 46, 47, 48, 49, 50, 51, 52, 53, 54] to mention a few).

A more classical approach in computational electrocardiology, also able to reduce the computational costs, relies on the Monodomain model. This is actually a model reduction of the Bidomain equations formulated in terms of the transmembrane potential (the difference between intra- and extra-cellular voltages), under the assumption that the anisotropy of the intra- and extra-cellular spaces is the same, i.e., the conductivity in the extra-cellular region is proportional to the intra-cellular conductivity. Even if this assumption is generally not completely justified, this model has been recognized as a possible trade-off between accuracy and efficiency. Besides, it gains the same level of information in the case of physiological spatio-temporal propagation (i.e., the object of the present study). For this reason, in this paper, we focus on the Monodomain system, coupled, in particular, with the simplified two-variable phenomenological *Rogers-McCulloch* (RM) model [14], featuring a single gating variable. More complex models, both physiological and phenomenological, are available in the literature [17, 55, 56, 57]. However, the purpose of this work is to assess a methodological procedure, so we defer the extension to more complex models to future works.

The Monodomain equations we refer to read

$$\begin{cases} \partial_t u = \nabla \cdot (\boldsymbol{\sigma} \nabla u) - I_{ion}(u, w) + I_{app} & \text{in } Q, \\ \mathrm{d}_t w = g(u, w) & \text{in } Q, \end{cases} \tag{12}$$

with initial and boundary conditions

$$\begin{cases} u(\boldsymbol{x},0) = u_0(\boldsymbol{x}), \quad w(\boldsymbol{x},0) = w_0(\boldsymbol{x}) & \text{in } \Omega, \\ \boldsymbol{\sigma}\nabla u \cdot \mathbf{n} = 0 & \text{on } \partial Q, \end{cases} \tag{13}$$

with $Q = \Omega \times (0,T)$ the space-time domain with boundary $\partial Q = \partial\Omega \times [0,T]$; $[0,T]$ a fixed time interval; u the transmembrane potential ([mV]); w the gating variable characterizing the RM model; $\boldsymbol{\sigma}$ the conductivity tensor ([cm^2/ms]), in general function of the local coordinates, $\boldsymbol{x}$, and of the local fiber direction, $\boldsymbol{a}$; I_{ion} the total ionic current flowing through the cell membrane; g the kinetic dynamics of the ionic quantities; I_{app} the external stimulation current (e.g., electrical pacing or synaptic input); $\mathbf{n}$ the outward unit normal vector to the boundary $\partial\Omega$; U_0 and w_0 the initial value for the potential and for the gating variable, respectively. According to the standard notation, symbols ∂_t, d_t, ∇ and $\nabla\cdot$ represent the partial and total derivatives in time, the spatial gradient and divergence operator respectively. The Neumann-type boundary condition $(13)_2$, usually adopted in this context, mimics an insulated tissue [16]. In mathematical terms, Neumann-type conditions try to minimize the sensitivity of arbitrary data on the simulation results [58].

We assume the computational domain Ω to be homogeneous and anisotropic, meaning that the conductivity tensor $\boldsymbol{\sigma}$ is uniform in space. Also this assumption will be removed in future works [25]. We define with $\{\boldsymbol{a}_l, \boldsymbol{a}_t, \boldsymbol{a}_n\}$ the orthonormal fields related to the structure of the myocardium which define the longitudinal, transverse and normal direction of the fibers, respectively [59, 16]. Accordingly, we identify with $(\sigma_l, \sigma_t, \sigma_n)$ the longitudinal, transverse and normal conductivity parameters. In the most general form, the conductivity tensor can be decomposed as

$$\boldsymbol{\sigma} = \sigma_l \boldsymbol{a}_l \boldsymbol{a}_l^T + \sigma_t \boldsymbol{a}_t \boldsymbol{a}_t^T + \sigma_n \boldsymbol{a}_n \boldsymbol{a}_n^T. \tag{14}$$

Moreover, for $d = 3$ and under the hypothesis of axial isotropy, i.e., $\sigma_t = \sigma_n$ and $\boldsymbol{a}_n \equiv \boldsymbol{e}_3$ with $\{\boldsymbol{e}_1, \boldsymbol{e}_2, \boldsymbol{e}_3\}$ the canonical basis in $\mathbb{R}^3$, the conductivity tensor reduces to

$$\boldsymbol{\sigma} = \sigma_t \mathbf{I} + (\sigma_l - \sigma_t)\boldsymbol{a}_l \boldsymbol{a}_l^T, \tag{15}$$

with $\mathbf{I} \in \mathbb{R}^{3\times 3}$ the identity tensor. The conductivity values belong to separate admissible intervals, namely, $\sigma_l \in [m_l, M_l]$ and $\sigma_t \in [m_t, M_t]$, $\Delta_l = M_l - m_l$ and $\Delta_t = M_t - m_t$ denoting the corresponding length, with $M_t < m_l$. In fact, it is observed that electrical conduction along the length of myocytes is faster than along the transverse direction [60, 61], so that σ_l should be greater than σ_t.

Let $\theta : \Omega \to [0, 2\pi]$ be the angle between the longitudinal fiber direction, $\boldsymbol{a}_l$, and the x-axis direction, $\boldsymbol{e}_1$, at any point of the domain Ω. It holds that $\boldsymbol{a}_l = (\cos\theta)\boldsymbol{e}_1 + (\sin\theta)\boldsymbol{e}_2$. Therefore, the conductivity tensor

RM parameters					
G	V_{th}	V_p	η_1	η_2	η_3
1.5 Ω^{-1}cm^{-2}	13 mV	100 mV	4.4 Ω^{-1}cm^{-2}	0.012 ms^{-1}	1 ms^{-1}

Table 1: Rogers-McCulloch model parameters. Here Ω denotes the Ohm, the unit of electrical resistance.

explicitly reads

$$\boldsymbol{\sigma} = \begin{bmatrix} \sigma_l \cos^2\theta + \sigma_t \sin^2\theta & (\sigma_l - \sigma_t)\cos\theta\sin\theta & 0 \\ (\sigma_l - \sigma_t)\cos\theta\sin\theta & \sigma_l \sin^2\theta + \sigma_t \cos^2\theta & 0 \\ 0 & 0 & \sigma_t \end{bmatrix} \quad \text{for } d = 3, \tag{16}$$

and

$$\boldsymbol{\sigma} = \begin{bmatrix} \sigma_l \cos^2\theta + \sigma_t \sin^2\theta & (\sigma_l - \sigma_t)\cos\theta\sin\theta \\ (\sigma_l - \sigma_t)\cos\theta\sin\theta & \sigma_l \sin^2\theta + \sigma_t \cos^2\theta \end{bmatrix} \quad \text{for } d = 2. \tag{17}$$

The RM model is based on a cubic polynomial formulation for I_{ion} and one gating variable which allow to describe the most relevant feature of the cardiac action potential at a limited computational cost. The model reads

$$I_{ion}(u,w) = Gu\left(1 - \frac{u}{V_{th}}\right)\left(1 - \frac{u}{V_p}\right) + \eta_1 uw, \qquad g(u,w) = \eta_2\left(\frac{u}{V_p} - \eta_3 w\right). \tag{18}$$

The parameters $G, V_{th}, V_p, \eta_1, \eta_2, \eta_3$ are provided in Table 1.

3.2. The Monodomain Inverse Conductivity Problem

The ultimate goal of our research stems from the clinical need of identifying the cardiac conductivities, σ_l, σ_t, in a patient-specific setting. This problem presents several practical challenges, for the limited access to data *in vivo*. Also, the available literature in the field shows that the range of these parameters may be quite large [62, 63, 64], while the numerical sensitivity of the Monodomain solution to cardiac conductivities is generally high [65].

A variational data assimilation approach was proposed and analyzed in [21, 23]. The basic idea is to infer the conductivities from available measures of the transmembrane potential retrieved from the surface of the tissue at certain instants of the propagation. The variational procedure achieves this assimilation by finding the conductivities that minimize the mismatch between the available data and the results of the Monodomain solution. Formally, this leads to the so-called *Monodomain Inverse Conductivity Problem* (MICP): find σ_l and σ_t in the tensor $\boldsymbol{\sigma}$ to minimize the functional

$$\mathcal{J}(\boldsymbol{\sigma}) = \frac{1}{2}\int_0^T \int_{\Omega_{obs}} (u(\boldsymbol{\sigma}) - u_{meas})^2 \, d\boldsymbol{x}dt, \tag{19}$$

subject to (12)-(13). Specifically, u_{meas} denotes the experimental data measured on the observation domain, $\Omega_{obs} \subset \Omega$, and u is function of $\boldsymbol{\sigma}$ through the (12,13,18)..

An existence analysis for this problem is reported in [23], whereas numerical and experimental validations are extensively discussed in [24, 25]. As it is promptly realized, the iterative minimization procedure based on the introduction of Lagrange multipliers and the solution of the Monodomain adjoint problem is computationally demanding. As a matter of fact, when following an optimize-then-discretize approach, we need to evaluate the Monodomain system and its adjoint, forward and backward in time, at each minimization iteration. This led to the introduction of model reduction techniques, based either on a Proper Orthogonal Decomposition (POD) paradigm [26, 28, 29] or the Lax-pairs [27]. The POD paradigm requires the offline computation of snapshots for different values of the parameters. Successively, these snapshots are reduced via SVD and combined to form a basis for a rapid evaluation of the solution for new values of the parameters. As demonstrated in [29], the selection of the snapshots is critical for the successful achievement of an efficient reduced solution, and specific techniques are required [28].

On the contrary, as already pointed out, the PGD approach does not need the computation of any snapshot in the offline phase, and directly computes the solution in the incremented independent-variable space (in our case, the extended independent variables are the space, the time and the two conductivities). The actual performance of PGD will be illustrated in the next section.

4. PGD Model Reduction of the Monodomain Problem

4.1. Formulation of the Reduced Model

To solve the Monodomain system with the PGD approach, we perform first a semi-discretization in time of the problem. This is, a priori, not necessary, as the time could be considered as an independent variable of the problem (like the space and the conductivities). However, we prefer to eliminate the time dependence by resorting to a traditional finite difference discretization. Also, we decouple the PDE from the ODE ionic model. By defining a time step $\Delta t > 0$, the time interval $[0, T]$ is uniformly divided into N subintervals, (t^n, t^{n+1}), with $t^0 = 0$, $t^N = T$, being $t^{n+1} = t^n + \Delta t = (n+1)\Delta t$, for any $n = 0, \ldots, N-1$. A popular strategy for the semi-discretization in time is a semi-implicit approach that automatically linearizes the problem at each time step. With this approach and using a first order discretization in time, at each time t^{n+1}, for (u^n, w^n) available, we solve the problems

$$\begin{cases} w^{n+1} = \Delta t\, g(u^n, w^{n+1}) + w^n \quad \text{in } \Omega, \\ u^{n+1} - \Delta t\, \nabla \cdot (\boldsymbol{\sigma} \nabla u^{n+1}) = \Delta t\, I_{app}^{n+1} - \Delta t\, I_{ion}(u^n, w^{n+1}) + u^n \quad \text{in } \Omega, \end{cases} \tag{20}$$

completed by the boundary conditions $(13)_2$. For each $n = 0, \dots, N-1$, (18,20) lead to

$$w^{n+1} = \frac{\eta_2 \Delta t}{(1 + \Delta t\, \eta_2 \eta_3) V_p} u^n + \frac{w^n}{1 + \Delta t\, \eta_2 \eta_3}. \tag{21}$$

Consequently, the ionic term reads

$$I_{ion}(u^n, w^{n+1}) = G u^n - G\left(\frac{1}{V_p} + \frac{1}{V_{th}}\right)(u^n)^2 + \frac{G}{V_p V_{th}}(u^n)^3 + \eta_1 u^n w^{n+1}. \tag{22}$$

At each step, we apply the PGD model reduction to $(20)_2$, whose weak formulation, for $V = H^1(\Omega)$, reads

$$a_{\boldsymbol{\sigma}}(u^{n+1}, v) = F_{\boldsymbol{\sigma}}(v) \quad \forall v \in V, \tag{23}$$

with

$$a_{\boldsymbol{\sigma}}(u^{n+1}, v) = \int_\Omega \Delta t\, \boldsymbol{\sigma} \nabla u^{n+1} \cdot \nabla v \, \mathrm{d}\Omega + \int_\Omega u^{n+1} v \, \mathrm{d}\Omega, \tag{24}$$

$$F_{\boldsymbol{\sigma}}(v) = \int_\Omega (\Delta t\, I_{app}^{n+1} - \Delta t\, I_{ion}(u^n, w^{n+1}) + u^n) v \, \mathrm{d}\Omega. \tag{25}$$

Notice that, for the sake of generality, we retain the index $\boldsymbol{\sigma}$ for the functional F in (23) to be consistent with our notation in Section 2. In fact, in our specific problem, the functional at the right hand side is independent of the parameters.

To apply the PGD approach, we introduce the space $W \equiv H^1(\Omega) \otimes L^2(\mathcal{S}_l) \otimes L^2(\mathcal{S}_t)$, where $\mathcal{S}_l$ and $\mathcal{S}_t$ are the admissible ranges for σ_l and σ_t, respectively. Then, the extended variational formulation (2) features

$$\mathcal{A}(u, v) = \int_{\mathcal{S}_l} \int_{\mathcal{S}_t} a_{\boldsymbol{\sigma}}(u, v) \, \mathrm{d}\sigma_l \, \mathrm{d}\sigma_t, \quad \mathcal{F}(v) = \int_{\mathcal{S}_l} \int_{\mathcal{S}_t} F_{\boldsymbol{\sigma}}(v) \, \mathrm{d}\sigma_l \, \mathrm{d}\sigma_t. \tag{26}$$

Again, we preserve the same notation, u and v, despite the dependence on σ_l and σ_t. To perform the model reduction, we introduce the PGD space

$$W_m = \left\{ w_m(\boldsymbol{x}; \sigma_l, \sigma_t) = \sum_{k=1}^{m} w_k^{\boldsymbol{x}}(\boldsymbol{x}) w_k^{\sigma_l}(\sigma_l) w_k^{\sigma_t}(\sigma_t), \text{ with } w_k^{\boldsymbol{x}} \in V_h,\, w_k^{\sigma_l} \in Q_h^{\sigma_l},\, w_k^{\sigma_t} \in Q_h^{\sigma_t},\, \boldsymbol{x} \in \Omega,\, \sigma_l \in \mathcal{S}_l, \sigma_t \in \mathcal{S}_t \right\}, \tag{27}$$

with V_h, $Q_h^{\sigma_l}$ and $Q_h^{\sigma_t}$ discrete subspaces of V, $L^2(\mathcal{S}_l)$ and $L^2(\mathcal{S}_t)$. The PGD approximation for the solution

at time $t = t^{n+1}$ is defined as

$$u^{n+1}(\boldsymbol{x};\sigma_l,\sigma_t) \approx \sum_{k=1}^{m_u^{n+1}} u_k^{n+1,\boldsymbol{x}}(\boldsymbol{x}) u_k^{n+1,\sigma_l}(\sigma_l) u_k^{n+1,\sigma_t}(\sigma_t). \tag{28}$$

We observe that the modal index m_u^{n+1} may vary, a priori, at each time-step. The different contributions of the sum are computed up to the fulfillment of criterion (8), while each term $u_k^{n+1,\boldsymbol{x}}$, u_k^{n+1,σ_l}, u_k^{n+1,σ_t}, is computed by the ADS strategy, breaking the solution into an iterative fixed-point solver, and alternatively solving for $\boldsymbol{x}$, σ_l and σ_t, as described in Section 2.

The factorization of the forms $\mathcal{A}$ and $\mathcal{F}$ in (5) leads to

$$\mathcal{A}(u,v) = \sum_{\alpha=1}^{10} a_\alpha^{\boldsymbol{x}}(u_\psi^{\boldsymbol{x}}, v_\beta^{\boldsymbol{x}}) a_\alpha^l(u_\psi^l, v_\beta^l) a_\alpha^t(u_\psi^t, v_\beta^t), \quad \mathcal{F}(v) = \sum_{\alpha=1}^{N_F} F_\alpha^{\boldsymbol{x}}(v_\beta^{\boldsymbol{x}}) F_\alpha^l(v_\beta^l) F_\alpha^t(v_\beta^t), \tag{29}$$

with ψ and β varying in the corresponding modal index range, and where the bilinear and linear factors are explicitly provided in Table 2 and 3, respectively. The notation $(\cdot,\cdot)$ stands for the standard L^2-product in Ω. For all the details concerning the derivation of the quantities in Tables 2 and 3, we refer to [66]. In particular, the factorization of the linear functional $\mathcal{F}(v)$ demands a separated representation also for w, given by

$$w^{n+1}(\boldsymbol{x};\sigma_l,\sigma_t) \approx \sum_{k=1}^{m_w^{n+1}} w_k^{n+1,\boldsymbol{x}}(\boldsymbol{x}) w_k^{n+1,\sigma_l}(\sigma_l) w_k^{n+1,\sigma_t}(\sigma_t), \tag{30}$$

although, in practice, the gating variable is computed via equation (21).

By a direct computation for N_F in (29), one verifies that

$$\begin{aligned} N_F &= 1 + 2m_u + 2\binom{m_u}{1} + 3\binom{m_u}{2} + \binom{m_u}{3} + m_u m_w \\ &= 1 + 4m_u + \frac{3}{2}m_u(m_u-1) + \frac{1}{6}m_u(m_u-1)(m_u-2) + m_u m_w, \end{aligned}$$

the time index being omitted to simplify notation. Actually, in (25), I_{app} contributes with a unique function, while the term u^n requires m_u functions. For the ionic term (22), the linear term requires m_u functions, the quadratic contribution demands $\binom{m_u}{1} + \binom{m_u}{2}$ functions, the cubic term leads to $\binom{m_u}{1} + 2\binom{m_u}{2} + \binom{m_u}{3}$ functions and the mixed term, in u^n and w^{n+1}, $m_u m_w$ functions. Finally, we remark that while N_a (equal to 10 in (29)) only depends on the differential terms identifying the bilinear form $\mathcal{A}$ and remains unchanged during the PGD iterations and in time, N_F changes during the enrichment iterations and, additionally, it changes in time, due to the time dependence in $F_{\boldsymbol{\sigma}}$.

Exploiting factorizations (28) and (29) in the inner loop (9)-(10), the generic fixed-point iteration, j, of the

Table 2: Factorization of the PGD extended bilinear form in (26). Lines for $\alpha = 1, \dots, 9$ refer to the second order term in (24), while the last line ($\alpha = 10$), refers to the reactive contribution.

α	$a^{\boldsymbol{x}}_\alpha(u^{\boldsymbol{x}}_\psi, v^{\boldsymbol{x}}_\beta)$	$a^l_\alpha(u^l_\psi, v^l_\beta)$	$a^t_\alpha(u^t_\psi, v^t_\beta)$
1	$\Delta t(\cos^2(\theta)\partial_x u^{\boldsymbol{x}}_\psi, \partial_x v^{\boldsymbol{x}}_\beta)$	$(\sigma_l u^l_\psi, v^l_\beta)$	(u^t_ψ, v^t)
2	$\Delta t(\sin^2(\theta)\partial_x u^{\boldsymbol{x}}_\psi, \partial_x v^{\boldsymbol{x}}_\beta)$	(u^l_ψ, v^l_β)	$(\sigma_t u^t_\psi, v^t_\beta)$
3	$\Delta t(\cos(\theta)\sin(\theta)\partial_y u^{\boldsymbol{x}}_\psi, \partial_x v^{\boldsymbol{x}}_\beta)$	$(\sigma_l u^l_\psi, v^l_\beta)$	(u^t_ψ, v^t_β)
4	$-\Delta t(\cos(\theta)\sin(\theta)\partial_y u^{\boldsymbol{x}}_\psi, \partial_x v^{\boldsymbol{x}}_\beta)$	(u^l_ψ, v^l_β)	$(\sigma_t u^t_\psi, v^t_\beta)$
5	$\Delta t(\cos(\theta)\sin(\theta)\partial_x u^{\boldsymbol{x}}_\psi, \partial_y v^{\boldsymbol{x}}_\beta)$	$(\sigma_l u^l_\psi, v^l_\beta)$	(u^t_ψ, v^t_β)
6	$-\Delta t(\cos(\theta)\sin(\theta)\partial_x u^{\boldsymbol{x}}_\psi, \partial_y v^{\boldsymbol{x}}_\beta)$	(u^l_ψ, v^l_β)	$(\sigma_t u^t_\psi, v^t_\beta)$
7	$\Delta t(\sin^2(\theta)\partial_y u^{\boldsymbol{x}}_\psi, \partial_y v^{\boldsymbol{x}}_\beta)$	$(\sigma_l u^l_\psi, v^l_\beta)$	(u^t_ψ, v^t_β)
8	$\Delta t(\cos^2(\theta)\partial_y u^{\boldsymbol{x}}_\psi, \partial_y v^{\boldsymbol{x}}_\beta)$	(u^l_ψ, v^l_β)	$(\sigma_t u^t_\psi, v^t_\beta)$
9	$\Delta t(\partial_z u^{\boldsymbol{x}}_\psi, \partial_z v^{\boldsymbol{x}}_\beta)$	$(\sigma_l u^l_\psi, v^l_\beta)$	(u^t_ψ, v^t_β)
10	$(u^{\boldsymbol{x}}_\psi, v^{\boldsymbol{x}}_\beta)$	(u^l_ψ, v^l_β)	(u^t_ψ, v^t_β)

Table 3: Factorization of the PGD extended linear form in (26). The first column provides the number of components for any row. As for the indices, we have k, γ, $\zeta = 1, \dots, m^n_u$ and $\xi = 1, \dots, m^{n+1}_w$.

	$F^{\boldsymbol{x}}_\alpha(v^{\boldsymbol{x}}_\beta)$	$F^l_\alpha(v^l_\beta)$	$F^t_\alpha(v^t_\beta)$	
1	$\Delta t(I^{n+1}_{app}, v^{\boldsymbol{x}}_\beta)$	$(1, v^l_\beta)$	$(1, v^t_\beta)$	
m_u	$(u^{n,\boldsymbol{x}}_k, v^{\boldsymbol{x}}_\beta)$	$(u^{n,\sigma_l}_k, v^l_\beta)$	$(u^{n,\sigma_t}_k, v^t_\beta)$	
m_u	$-\Delta t G(u^{n,\boldsymbol{x}}_k, v^{\boldsymbol{x}}_\beta)$	$(u^{n,\sigma_l}_k, v^l_\beta)$	$(u^{n,\sigma_t}_k, v^t_\beta)$	
m_u	$\Delta t G(\frac{1}{V_p} + \frac{1}{V_{th}})((u^{n,\boldsymbol{x}}_k)^2, v^{\boldsymbol{x}}_\beta)$	$((u^{n,\sigma_l}_k)^2, v^l_\beta)$	$((u^{n,\sigma_t}_k)^2, v^t_\beta)$	
$\binom{m_u}{2}$	$2\Delta t G(\frac{1}{V_p} + \frac{1}{V_{th}})(u^{n,\boldsymbol{x}}_k u^{n,\boldsymbol{x}}_\gamma, v^{\boldsymbol{x}}_\beta)$	$(u^{n,\sigma_l}_k u^{n,\sigma_l}_\gamma, v^l_\beta)$	$(u^{n,\sigma_t}_k u^{n,\sigma_t}_\gamma, v^t_\beta)$	with $\gamma > k$
m_u	$-\Delta t \frac{G}{V_p V_{th}}((u^{n,\boldsymbol{x}}_k)^3, v^{\boldsymbol{x}}_\beta)$	$((u^{n,\sigma_l}_k)^3, v^l_\beta)$	$((u^{n,\sigma_t}_k)^3, v^t_\beta)$	
$2\binom{m_u}{2}$	$-3\Delta t \frac{G}{V_p V_{th}}((u^{n,\boldsymbol{x}}_k)^2 u^{n,\boldsymbol{x}}_\zeta, v^{\boldsymbol{x}}_\beta)$	$((u^{n,\sigma_l}_k)^2 u^{n,\sigma_l}_\zeta, v^l_\beta)$	$((u^{n,\sigma_t}_k)^2 u^{n,\sigma_t}_\zeta, v^t_\beta)$	with $\zeta \neq k$
$\binom{m_u}{3}$	$-6\Delta t \frac{G}{V_p V_{th}}(u^{n,\boldsymbol{x}}_k u^{n,\boldsymbol{x}}_\zeta u^{n,\boldsymbol{x}}_\gamma, v^{\boldsymbol{x}}_\beta)$	$(u^{n,\sigma_l}_k u^{n,\sigma_l}_\zeta u^{n,\sigma_l}_\gamma, v^l_\beta)$	$(u^{n,\sigma_t}_k u^{n,\sigma_t}_\zeta u^{n,\sigma_t}_\gamma, v^t_\beta)$	with $\gamma > \zeta > k$
$m_u m_w$	$\Delta t \eta_1(u^{n,\boldsymbol{x}}_k w^{n+1,\boldsymbol{x}}_\xi, v^{\boldsymbol{x}}_\beta)$	$(u^{n,\sigma_l}_k w^{n+1,\sigma_l}_\xi, v^l_\beta)$	$(u^{n,\sigma_t}_k w^{n+1,\sigma_t}_\xi, v^t_\beta)$	

three-step ADS reads

$$
\begin{cases}
\displaystyle\sum_{\alpha=1}^{10} \mathbf{a}_\alpha^{\boldsymbol{x}}(\mathbf{u}_{\mathbf{m,j}}^{\mathbf{n+1},\boldsymbol{x}}, \mathbf{v}_{\mathbf{m}}^{\boldsymbol{x}}) a_\alpha^l(u_{m,j-1}^{n+1,\sigma_l}, u_{m,j-1}^{n+1,\sigma_l}) a_\alpha^t(u_{m,j-1}^{n+1,\sigma_t}, u_{m,j-1}^{n+1,\sigma_t}) = \sum_{\alpha=1}^{N_F} F_\alpha^{\boldsymbol{x}}(v_m^{\boldsymbol{x}}) F_\alpha^l(u_{m,j-1}^{n+1,\sigma_l}) F_\alpha^t(u_{m,j-1}^{n+1,\sigma_t}) \\
\quad - \displaystyle\sum_{\alpha=1}^{10}\sum_{k=1}^{m-1} a_\alpha^{\boldsymbol{x}}(u_k^{n+1,\boldsymbol{x}}, v_m^{\boldsymbol{x}}) a_\alpha^l(u_k^{n+1,\sigma_l}, u_{m,j-1}^{n+1,\sigma_l}) a_\alpha^t(u_k^{n+1,\sigma_t}, u_{m,j-1}^{n+1,\sigma_t}) \quad \forall v_m^{\boldsymbol{x}} \in V_h, \\
\displaystyle\sum_{\alpha=1}^{10} a_\alpha^{\boldsymbol{x}}(u_{m,j}^{n+1,\boldsymbol{x}}, u_{m,j}^{n+1,\boldsymbol{x}}) \mathbf{a}_\alpha^{\mathbf{l}}(\mathbf{u}_{\mathbf{m,j}}^{\mathbf{n+1},\sigma_\mathbf{l}}, \mathbf{v}_{\mathbf{m}}^{\mathbf{l}}) a_\alpha^t(u_{m,j-1}^{n+1,\sigma_t}, u_{m,j-1}^{n+1,\sigma_t}) = \sum_{\alpha=1}^{N_F} F_\alpha^{\boldsymbol{x}}(u_{m,j}^{n+1,\boldsymbol{x}}) F_\alpha^l(v_m^l) F_\alpha^t(u_{m,j-1}^{n+1,\sigma_t}) \\
\quad - \displaystyle\sum_{\alpha=1}^{10}\sum_{k=1}^{m-1} a_\alpha^{\boldsymbol{x}}(u_k^{n+1,\boldsymbol{x}}, u_{m,j}^{n+1,\boldsymbol{x}}) a_\alpha^l(u_k^{n+1,\sigma_l}, v_m^l) a_\alpha^t(u_k^{n+1,\sigma_t}, u_{m,j-1}^{n+1,\sigma_t}) \quad \forall v_m^l \in Q_h^{\sigma_l}, \\
\displaystyle\sum_{\alpha=1}^{10} a_\alpha^{\boldsymbol{x}}(u_{m,j}^{n+1,\boldsymbol{x}}, u_{m,j}^{n+1,\boldsymbol{x}}) a_\alpha^l(u_{m,j}^{n+1,\sigma_l}, u_{m,j}^{n+1,\sigma_l}) \mathbf{a}_\alpha^{\mathbf{t}}(\mathbf{u}_{\mathbf{m,j}}^{\mathbf{n+1},\sigma_\mathbf{t}}, \mathbf{v}_{\mathbf{m}}^{\mathbf{t}}) = \sum_{\alpha=1}^{N_F} F_\alpha^{\boldsymbol{x}}(u_{m,j}^{n+1,\boldsymbol{x}}) F_\alpha^l(u_{m,j}^{n+1,\sigma_l}) F_\alpha^t(v_m^t) \\
\quad - \displaystyle\sum_{\alpha=1}^{10}\sum_{k=1}^{m-1} a_\alpha^{\boldsymbol{x}}(u_k^{n+1,\boldsymbol{x}}, u_{m,j}^{n+1,\boldsymbol{x}}) a_\alpha^l(u_k^{n+1,\sigma_l}, u_{m,j}^{n+1,\sigma_l}) a_\alpha^t(u_k^{n+1,\sigma_t}, v_m^t) \quad \forall v_m^t \in Q_h^{\sigma_t},
\end{cases}
\tag{31}
$$

where, to simplify the notation, we have set $m_u^{n+1} = m$. Moreover, we have highlighted in bold the term each equation has to be solved for.

4.2. Implementation Details

For the discrete spaces V_h, $Q_h^{\sigma_l}$ and $Q_h^{\sigma_t}$ in (27) we choose piecewise linear finite elements (FE) [67]. At the time $t = t^{n+1}$, the initial guess for the external loop is set to $u_0^{n+1,\boldsymbol{x}} = u_0^{n+1,\sigma_l} = u_0^{n+1,\sigma_t} = 0$, whereas the contributions determined at the m-th ADS iteration are initially set to $u_{m,0}^{n+1,\boldsymbol{x}} = u_{m,0}^{n+1,\sigma_l} = u_{m,0}^{n+1,\sigma_t} = 1$ consistent with the Neumann-type boundary condition $(13)_2$. As for the tolerances tol_e and tol_i in Algorithm 1, we will select different values to investigate the impact of this choice on the performance of the PGD. The linear systems following the discretization of the three ADS steps in (31) are solved using the conjugate gradient method with a standard incomplete LU (ILU) right preconditioner [68]. While this strategy is appropriate to solve the first ADS step, $(31)_1$, that may lead to large linear systems associated with the discretization of the physical space, the remaining steps concern the parametric space and, in general, they require the solution of smaller linear systems. Direct solvers may be more efficient in such cases, depending on the linear algebra package used. The optimization of this part of the implementation will be object of future works. Simulations were carried out in serial, on a workstation equipped with Intel 6-Core i7-7800X CPU 3.50GHz and 64 GB of RAM. The code was implemented in LifeV [69, 70], an object oriented C++ parallel finite element library based on the Trilinos project [71], developed by different groups worldwide.

4.3. Numerical Results for the Reduction of the Forward Problem

Here we investigate the performance of the PGD technique to reduce the Monodomain model (12) in terms of accuracy of the solution and computational efficiency. We focus on realistic geometries, both in 2D and 3D.

4.3.1. A 2D Canine Tissue Geometry

We consider a realistic 2D geometry of a portion of a canine ventricular tissue [72]. The computational domain features 22747 degrees of freedom (DOFs). Fig. 1(a) shows the mesh and the cardiac fiber structure that was roughly approximated by looking at the anatomy of the tissue. As previously mentioned, the cardiac tissue is assumed homogeneous, so that the conductivity fields are constant and identified by the 2D vector $\boldsymbol{\sigma} = (\sigma_l, \sigma_t)$ with the local preferred orientation represented in the right panel of Fig. 1(a). The parameters, σ_l and σ_t, belong to the admissible space $\mathcal{S} = \mathcal{S}_l \times \mathcal{S}_t = [m_l, M_l] \times [m_t, M_t] = [0.06, 0.09]\,\mathrm{cm}^2/\mathrm{ms} \times [0.01, 0.04]\,\mathrm{cm}^2/\mathrm{ms}$, ($\Delta_l = \Delta_t = 0.03$ $\mathrm{cm}^2/\mathrm{ms}$). These bounds were manually tuned so to reproduce the realistic wavefront propagation velocities observed *in vitro* experiments [72, 73]. Domain $\mathcal{S}$ has been discretized with 250×250 DOFs, while the simulation time step is set to $\Delta t = 0.2$ ms until $T = 30$ ms. One stimulus of $I_{app} = 250$ mV/ms is applied at the top of the domain for a duration of 2 ms. For the sake of the computational costs, we focus on the wavefront propagation, whereas insights into the PGD approximation for the whole action potential are provided in Appendix A.

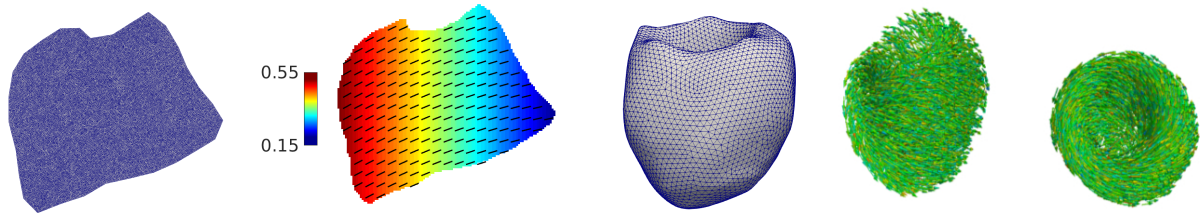

(a) (b)

Figure 1: (a) Realistic geometry of a 2D portion of a canine ventricular tissue: computational mesh (left) and approximation of the fiber structure (right). The segments represent the local cardiac fiber direction, while the colorbar indicates the value of the local fiber angle with respect to the x-axis (unit of measurement is in radians). (b) 3D mesh (left) and myocardial fiber orientation from two different viewpoints (center-right) for the real ventricle simulation (image from [23]).

One of the primary goals of the following numerical experiments is to investigate the interplay between the tolerance tol_e (associated to the number of modes) and the reliability of the solution. In fact, the lower the tolerance, the more accurate is expected to be the PGD solution. However, this entails higher computational costs in the offline phase as more modes are required to converge. We compare the full FE Monodomain solution, assumed as the reference solution, with the PGD approximation, varying tol_e=10^{-4}, 10^{-5},10^{-6}, and the conductivities. The tolerance of the ADS fixed point iterations, tol_i, is set to 10^{-2}.

Fig. 2(a) shows the number of modes as a function of the time. We notice that more modes are needed as the excitable wave travels through the tissue and the dynamics become more involved. Then, this number suddenly drops at around t=22 ms, when the wavefront propagation terminates. As expected, the number of modes needed for convergence increases with lower tolerance values. This results in a heavier computational burden of the offline phase, as highlighted in Table 4. However, the computation of the PGD solution in the

	10^{-4}	10^{-5}	10^{-6}	FE
Offline [h]	0.9	4.6	30.5	/
Online [s]	0.1	0.15	0.2	15

Table 4: 2D canine tissue: CPU times of the PGD approach for different values of tol_e, and time demanded by the FE solver.

online phase is remarkably inexpensive. Evaluating the PGD approximation at a new pair of parameters, (σ_l, σ_t), only takes at most 0.2 s in contrast with 15 s of the corresponding FE solution, thus reducing the computation time of two orders of magnitude. The easy evaluation of the PGD solution is extremely helpful to set up a fast solver for the inverse problem, as we will verify in the next section.

In terms of accuracy, the quality of the PGD solution depends on the conductivity values which, in this particular case where we do not perform any change in the model reaction parameters, are mostly determined by the parameter σ_t. Fig. 2(b) displays the percentage L^2-relative error between the FE and the PGD transmembrane potential obtained with tol_e=10^{-4}, σ_l = 0.09 cm^2/ms, and for σ_t = 0.01, 0.02, 0.03, 0.035, 0.04 cm^2/ms, corresponding to the conduction velocities (CVs) = 0.15, 0.21, 0.25, 0.27, 0.29 cm/ms, ordered from the lowest to the highest value. Regardless of the wavefront velocity, the discrepancy between the FE and the PGD approximation is minimal after the excitation ends. On the other hand, during the potential propagation, the error increases at faster CVs, reaching almost 40% for σ_t = 0.04 cm^2/ms. The accuracy of the PGD solution improves for slow CVs. For instance, for $\sigma_t = 0.01, 0.02$ cm^2/ms, the error is always below 10%. Therefore, we postulate that the PGD basis is informative enough to reproduce slow excitation waves, yet it needs further enrichment to accurately capture faster wavefront propagation. This is confirmed in Fig. 2(c) comparing the percentage L^2-relative error on the potential when reducing the tolerance. Also, let us introduce the *anisotropy ratio* R_a defined as $R_a \equiv \sigma_l/\sigma_t$. The solution of the Monodomain equation in known to be sensitive to R_a (see e.g. [29]), so we analyze three different values typical for the cardiac tissue [16], R_a = 2, 4, 6, corresponding to $\boldsymbol{\sigma}$ = $(0.07, 0.035)$ cm^2/ms, $\boldsymbol{\sigma}$ =$(0.08, 0.02)$ cm^2/ms and $\boldsymbol{\sigma}$ =$(0.084, 0.014)$ cm^2/ms, respectively. The case R_a = 2 features the highest CVs as σ_t takes the greatest value (0.035 cm^2/ms), whereas the cases R_a = 4, 6 result in a slower propagation. The approximation is overall inaccurate at the initial stages of the propagation because of the lack of regularity of the stimulus function I_{app} that abruptly goes to zero after 2 ms. Then, for the high CV case, R_a = 2, the maximum of the error decreases from roughly 20% for tol_e=10^{-4} to approximately 10% and 3% for tol_e=$10^{-5}, 10^{-6}$, respectively. Therefore, enriching the PGD basis is necessary to ensure a reasonable accuracy in the case of high CVs. For low CV cases, R_a = 4, 6, the approximation slightly improves in case of a richer PGD basis. However, setting tol_e=10^{-4} already guarantees a good approximation as the error is below 10%.

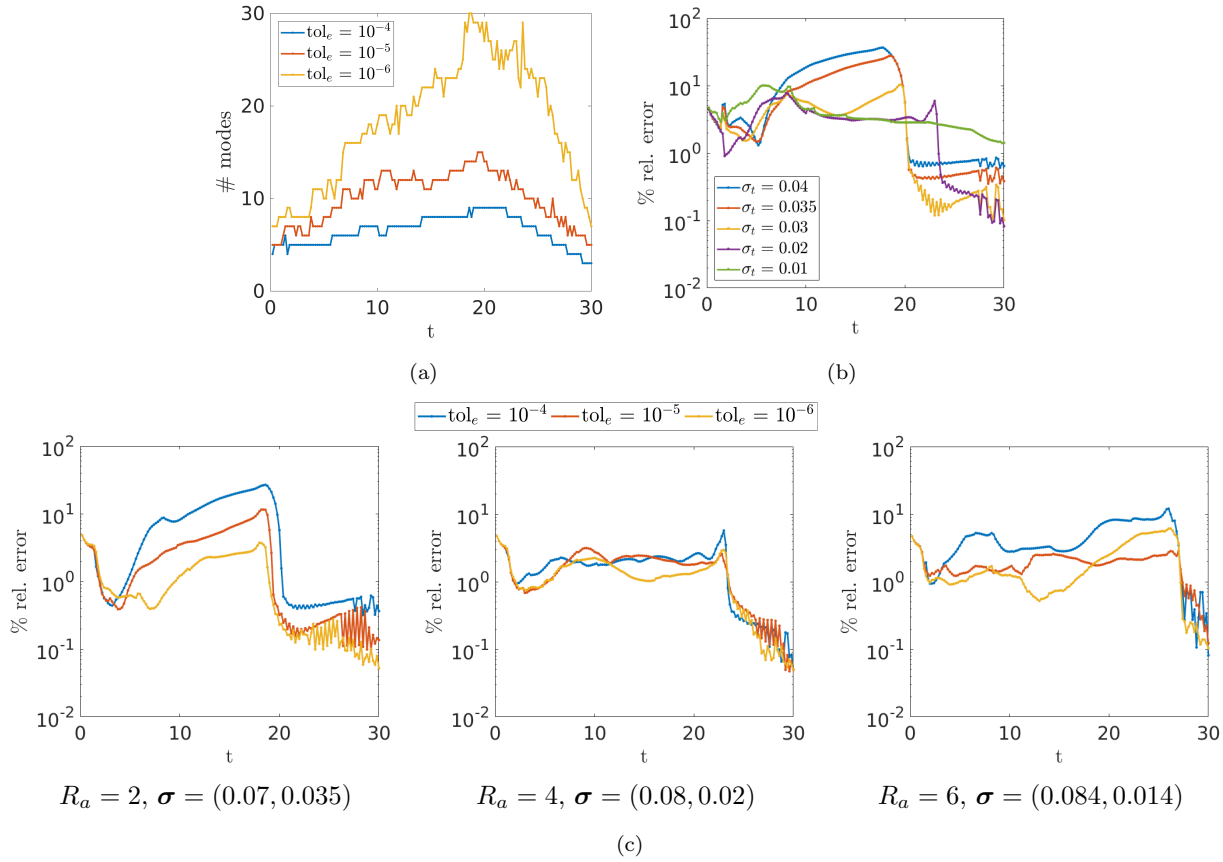

Figure 2: 2D canine tissue: (a) Trend of the PGD modes for different tolerances. (b) Percentage L^2-relative error between the FE and the PGD potential, for different conductivity values and $\text{tol}_e = 10^{-4}$. (c) Percentage L^2-relative error between the FE and the PGD potential for different tolerances and anisotropy ratios.

A qualitative comparison between FE and PGD transmembrane potentials varying tolerance tol_e and anisotropy ratio is provided in Fig. 3. The snapshots shown are related to the times featuring the highest error. As for the PGD solution obtained with tol_e=10^{-4}, the CVs are accurately captured for the slow CV cases, $R_a = 4, 6$ in (b) and (c), whereas, for the high CV case, $R_a = 2$ in (a), the PGD wavefront propagation is slower than the FE one, so that CV is underestimated. As expected, a smaller tolerance improves the accuracy, with an associated increment of the computational cost (compare the PGD solution for tol_e=10^{-6} with the FE approximation). In general, setting tol_e=10^{-5} seems to be the most convenient trade-off between accuracy and efficiency. The absolute value of the error between the FE and the PGD potential for the high CV case, $R_a = 2$, is shown in Fig. 4 for two different times. The error increases as the wavefront propagation approaches the boundary independently of the selected (external) tolerance, confirming the influence of the boundary conditions on the simulations [58].

An additional investigation aims at understanding the dependence of the accuracy on other parameters than the tolterance tol_e. Since tol_e=10^{-4} gives a good computational efficiency, we keep this value and explore possible ways to improve the quality of the resulting PGD approximation in case of high CVs by changing other numerical parameters. In particular, three strategies are investigated:

(a) refining the discretization of the admissible space $\mathcal{S}$;

(b) lowering the tolerance, tol_i, for the inner fixed point iterations;

(c) narrowing the admissible interval for σ_t since the CVs mostly depends on it.

The first two strategies attain at the selection of discretization parameters, while the third one refers to our *a priori* knowledge on the parameter to estimate.

For strategy (a), $\mathcal{S}$ is discretized with 500×500 as opposed to 250×250 DOFs used for the previous tests. Regarding (b), we test the accuracy of the PGD solution decreasing the tolerance, tol_i, from 10^{-2} to 10^{-4}. The percentage L^2-relative error on the potential yielded by strategies (a) and (b) is shown in Fig. 5(a) for $\boldsymbol{\sigma} = (0.07, 0.035)$ cm^2/ms. Both the approaches do not result in a lower approximation error. In fact, the refinement of the partition of $\mathcal{S}$ do not give any improvement, while a lower tolerance tol_i is slightly beneficial only in the initial stage of the wave propagation. We also notice that these two strategies entail higher computational costs, either for the size of each problem (strategy (a)) or the number of nternal iterations (strategy (b)).

On the other hand, approach (c) successfully reduces the error. In Fig. 5(b), we analyze the performance of PGD in terms of percentage L^2-relative error on the potential and number of modes, for $\Delta_t = 0.01$, 0.02 cm^2/ms, and compare this trend with the results obtained for $\Delta_t = 0.03$ cm^2/ms, Δ_l being set to 0.03 cm^2/ms. Narrower Δ_t yields an improvement of the PGD approximation, with $\Delta_t = 0.01$ cm^2/ms leading to the most accurate results (the error reduces from roughly 20% to 3%). This is reasonable since restricting

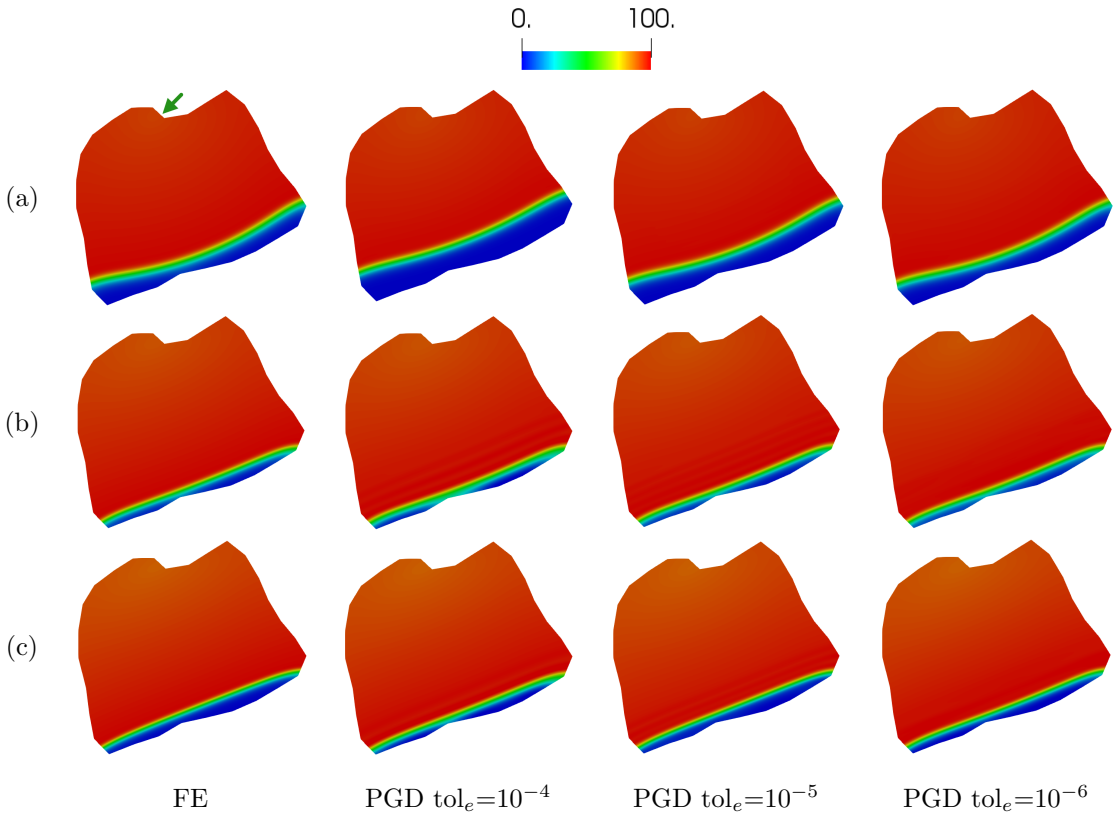

Figure 3: 2D canine tissue: FE and PGD solutions for different anisotropy ratios and tolerances. The green arrow in (a) points out the stimulation site. (a) $R_a = 2$, $\boldsymbol{\sigma} = (0.07, 0.035)$ cm^2/ms, $t = 17$ ms. (b) $R_a = 4$, $\boldsymbol{\sigma} = (0.08, 0.02)$ cm^2/ms, $t = 22$ ms. (c) $R_a = 6$, $\boldsymbol{\sigma} = (0.084, 0.014)$ cm^2/ms, $t = 25$ ms.

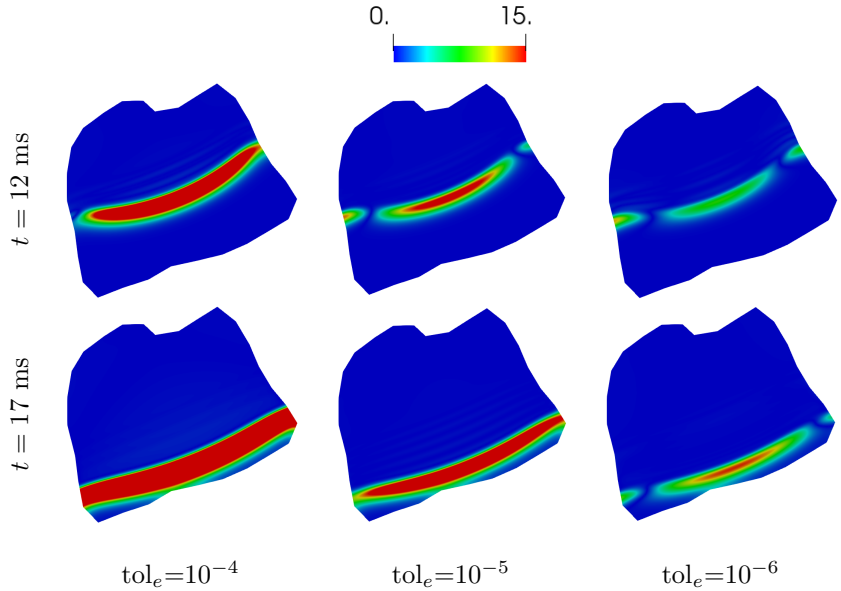

Figure 4: 2D canine tissue: distribution of the absolute value of the error on the potential [mV] between FE and PGD solutions for $R_a = 2$, $\boldsymbol{\sigma} = (0.07, 0.035)$ cm^2/ms for two different times.

the admissible interval for σ_t implies less values to explore. Therefore, the more *a priori* knowledge we have on the parameter values, the better the approximation becomes. Strategy (c) is also beneficial to efficiency, as fewer modes are needed for convergence thus containing the computational demand of the offline phase.

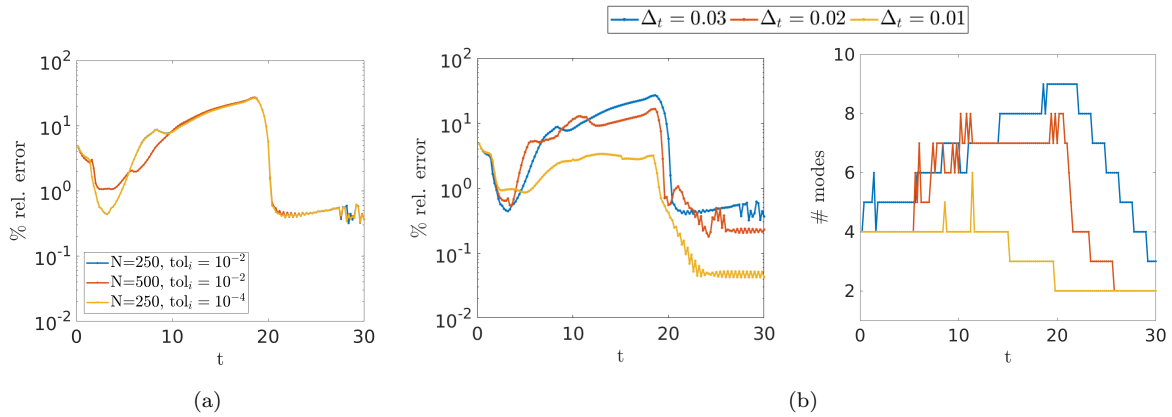

Figure 5: 2D canine tissue: possible improvements of PGD approximation with tol$_e$=10^{-4} in case of high CVs ($\boldsymbol{\sigma} = (0.07, 0.035)$ cm^2/ms). (a) Percentage L^2relative error on the potential when increasing the number of DOFs for the discretization of $\mathcal{S}$ versus when lowering tolerance tol$_i$. (b) Percentage L^2-relative error on the potential (left panel) and trend of the number of modes (right panel) when narrowing the admissible interval for σ_t.

4.3.2. A 3D Canine Tissue Geometry

To assess the impact of the geometry size on the quality and efficiency of the PGD, we consider a 3D canine tissue geometry obtained by extruding, along the z-axis, the 2D domain used in the previous section. The resulting mesh is 0.5 cm thick and discretized with 136482 DOFs. The cardiac fiber structure on the top surface of the mesh is the same as in the 2D case and then it is extruded along the z-axis. We consider the most general admissible space for the conductivity parameters $\mathcal{S} = [0.06, 0.09]\,\text{cm}^2/\text{ms} \times [0.01, 0.04]\,\text{cm}^2/\text{ms}$, discretized with 250×250 DOFs. As done in the 2D test, we analyze the anisotropy ratios $R_a = 2$, 4, 6 corresponding to $\boldsymbol{\sigma} = (0.07, 0.035)$ cm^2/ms, $\boldsymbol{\sigma} = (0.08, 0.02)$ cm^2/ms and $\boldsymbol{\sigma} = (0.084, 0.014)$ cm^2/ms, respectively. Having more degrees of freedom in the mesh of the domain when compared to the 2D case clearly results in an increment of the CPU time. Table 5 shows that the offline phase actually takes 8 and 41 hours for tol$_e$=10^{-4} and 10^{-5}, respectively. The case tol$_e$=10^{-6} considered in the 2D setting was not explored here because computationally unaffordable. As for the online phase, adopting the PGD technique is extremely convenient since the evaluation of the reduced solution requires at most 0.75 s as opposed to 330 s for the FE approximation.

As shown in Fig. 6, the trend of the error is rather similar to the 2D case, when varying the tolerance and the anisotropy ratio (compare with Fig. 2(c)). For tol$_e$=10^{-4}, the case $R_a = 2$, corresponding to high CVs, features higher error than for the other two values. Decreasing the tolerance to 10^{-5} qualitatively improves the solution.

	10^{-4}	10^{-5}	FE
Offline [h]	8	41	/
Online [s]	0.6	0.75	330

Table 5: 3D canine tissue: CPU times of the PGD approach for different values of tol_e, and time demanded by the FE solver.

A qualitative comparison between the FE and the PGD transmembrane potential for different tolerances and conductivities is carries out in Fig. 7. As already noted in the 2D experiment, in the high CV case, $R_a = 2$, the PGD solution obtained with tol_e=10^{-4} underestimates the CVs, yielding a poor approximation of the FE solution. On the contrary, in the cases $R_a = 4, 6$, although the CVs are slightly overestimated, the PGD solution is sufficiently close to the FE approximation. Overall, the PGD approximation improves for tol_e=10^{-5} providing a better matching of the wavefront propagation of the FE solution. Finally, we remark that the anisotropy ratio R_a does not have a significant impact on the accuracy of the PGD approach.

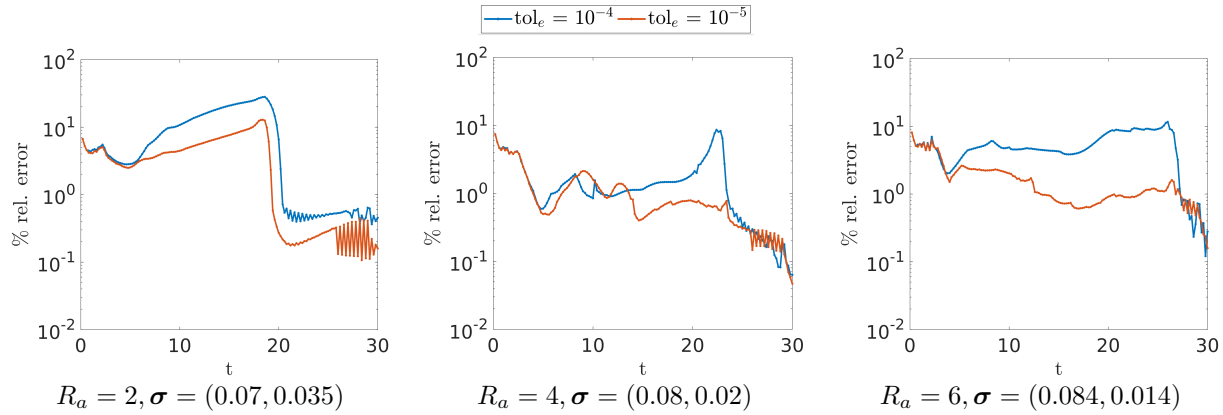

Figure 6: 3D canine tissue: percentage L^2-relative error between the FE and the PGD potential for different tolerances and anisotropy ratios.

4.3.3. A Real Ventricle

In view of clinical applications, we run simulations on a real left ventricular geometry reconstructed from SPECT images [44]. The excitation wave was simulated on a mesh with 22470 DOFs. Fig. 1(b) displays the 3D mesh and a realistic representation of the fiber structure used in the simulation. The fiber orientation was first obtained on an ellipsoidal domain and then adapted to the real domain, following the strategy proposed in [44]. The conductivity values are the same as in the previous tests. In this case, the resulting CVs are similar, whereas the influence of the anisotropy ratio R_a on the wavefront curvature is more evident. One stimulus of $I_{app} = 250$ mV/ms is applied at the ventricular endocardium, for a duration of 2 ms. The electrical propagation simulated with the FE method for $\boldsymbol{\sigma} = (0.08, 0.02)$ cm^2/ms is shown in Fig. 8. Since the adopted spatial discretization is coarser than the one used for the 3D canine geometry, we also included

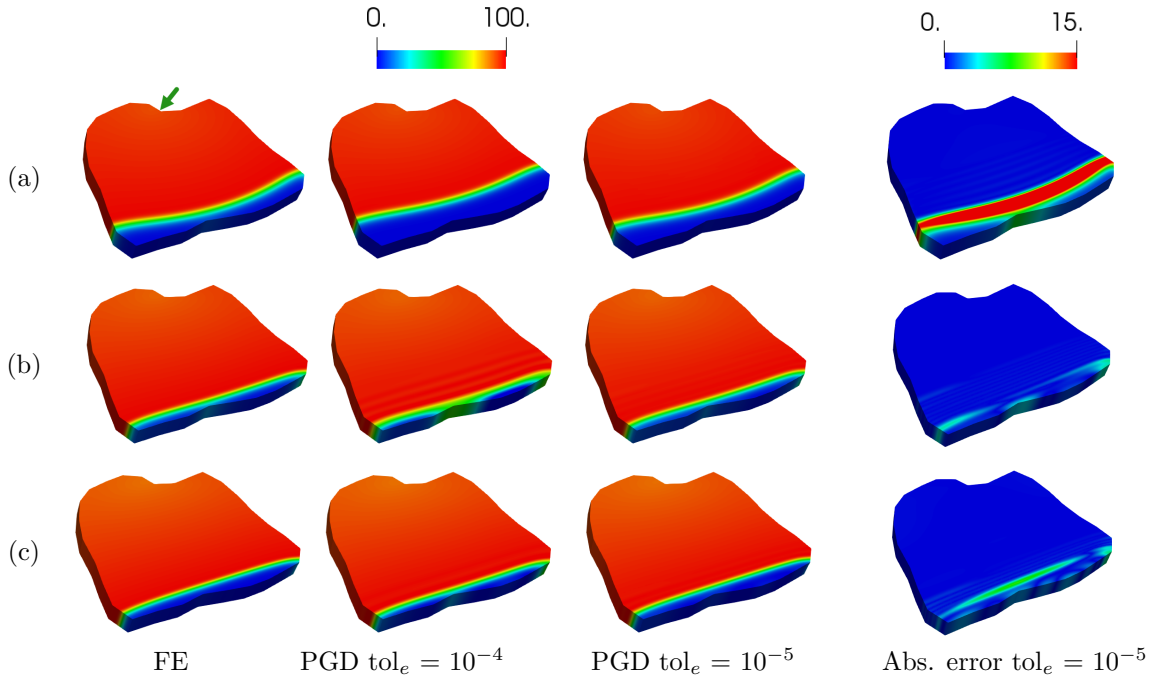

Figure 7: 3D canine tissue: FE and PGD solutions for different anisotropy ratios and tolerances (three left panels). The green arrow in (a) points out the stimulation site. (a) $R_a = 2$, $\boldsymbol{\sigma} = (0.07, 0.035)$ cm^2/ms, $t = 17$ ms. (b) $R_a = 4$, $\boldsymbol{\sigma} = (0.08, 0.02)$ cm^2/ms, $t = 22$ ms. (c) $R_a = 6$, $\boldsymbol{\sigma} = (0.084, 0.014)$ cm^2/ms, $t = 25$ ms. The right panel shows the distribution of the absolute value of the error on the potential [mV] between FE and PGD solutions.

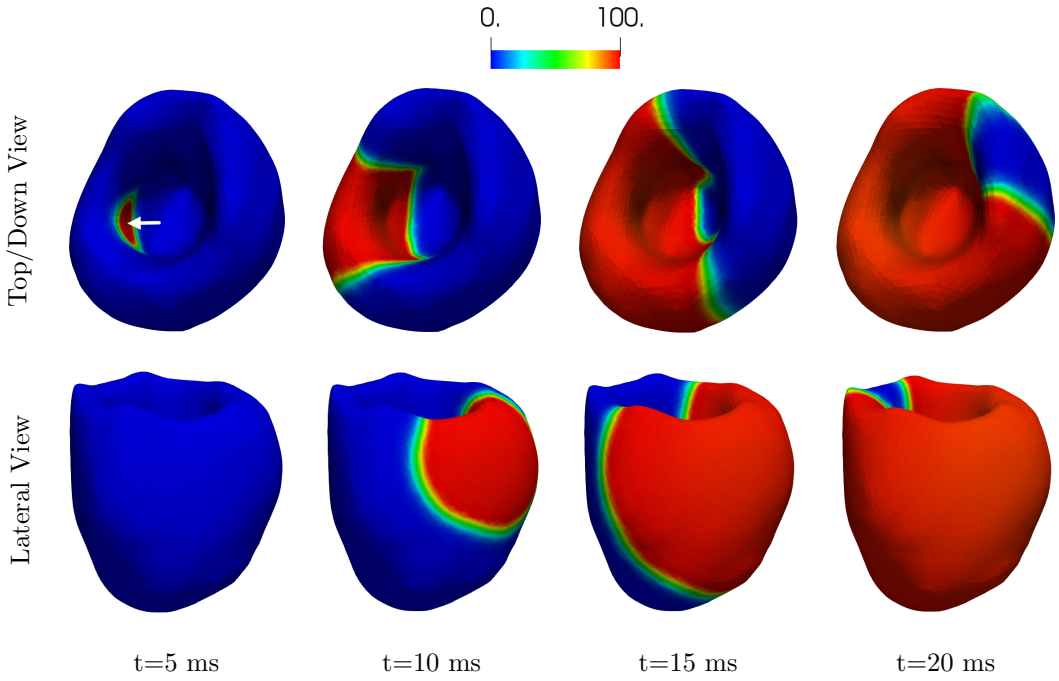

Figure 8: Real ventricle: snapshots of the excitation wave propagation (visualized from two different perspectives) simulated using the FE method. The white arrow in snapshot t=5 ms, (top) highlights the stimulation site triggering the propagation.

	10^{-4}	10^{-5}	10^{-6}	FE
Offline [h]	0.8	4.1	32	/
Online [s]	0.1	0.15	0.2	60

Table 6: Real ventricle: CPU times of the PGD approach for different values of tol_e, and time demanded by the FE solver.

tol_e=10^{-6} in our analysis. As shown in Table 6, the offline phase takes 0.8, 4.1 and 32 hours for tol_e=10^{-4}, 10^{-5}, 10^{-6}, respectively. On the other hand, we emphasize that the online phase is extremely inexpensive as it requires at most 0.2 s as opposed to 60 s of the FE simulation. The trend of the error on the potential between the FE and the PGD solution when varying the tolerance, tol_e, and the anisotropy ratio is displayed in Fig. 9. Unlike the previous tests, the three anisotropy ratios show a similar error for tol_e=10^{-4}, with a loss of accuracy for $R_a = 4, 6$ in comparison to the canine tissue tests. However, the approximation is overall reliable as the error is around 10%. The negative impact of the discontinuity of I_{app} on the accuracy of the PGD technique is more evident in these experiments as the error at the initial stage of the simulation is around 30%. The reliability of the approximation does not significantly benefit from lower tolerance values of tol_e. Only the case $R_a = 2$ presents a slight reduction of the error, although less significant than the tests with the canine geometry. For $R_a = 4$ and 6 we do not have substantial improvement. We argue that, in these cases, the accuracy is determined by the numerical errors of the space discretization and the linear systems solution.

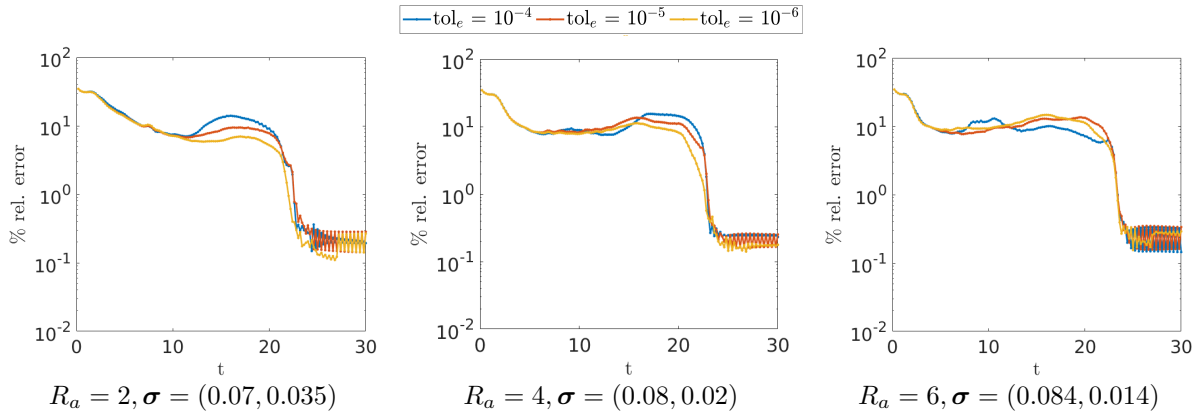

Figure 9: Real ventricle: percentage L^2-relative error between the FE and the PGD potential for different tolerances and anisotropy ratios.

The results are confirmed in Fig. 10 with a visual comparison of the different solutions. Notice that a higher error is observed at the ventricular apex, in particular in the cases $R_a = 4$, 6, because of the complex swirling pattern of the cardiac fibers and the geometric curvature of the ventricle that affect the accuracy of the simulations.

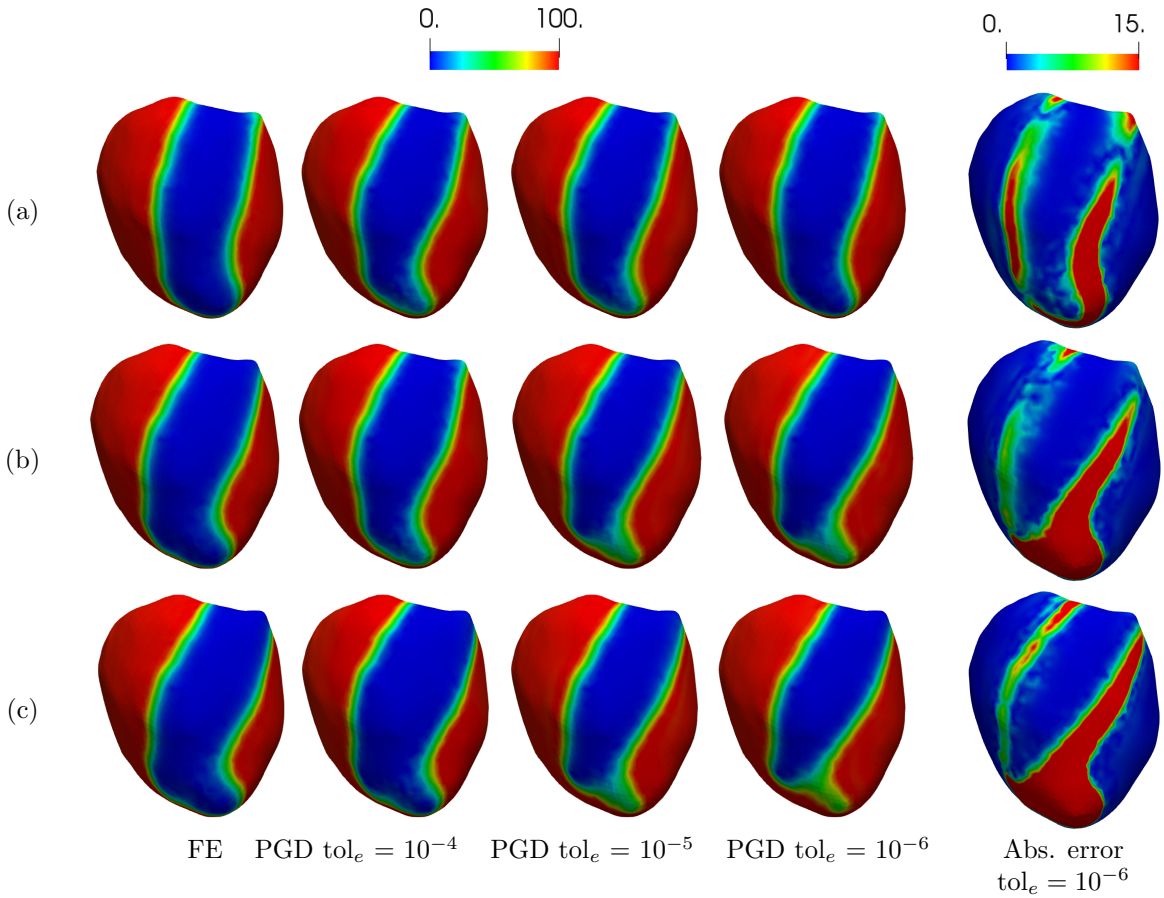

Figure 10: Real ventricle: FE and PGD solutions for different anisotropy ratios and tolerances (four left panels) at $t = 20$ ms. The stimulation point is located at the ventricular endocardium, thus it is not visible from this visual perspective. (a) $R_a = 2$, $\boldsymbol{\sigma} = (0.07, 0.035)$ cm^2/ms. (b) $R_a = 4$, $\boldsymbol{\sigma} = (0.08, 0.02)$ cm^2/ms. (c) $R_a = 6$, $\boldsymbol{\sigma} = (0.084, 0.014)$ cm^2/ms. The right panel shows the distribution of the absolute value of the error on the potential [mV] between FE and PGD solutions.

5. Solving the PGD-MICP

We verify now that PGD may significantly accelerate the minimization of the misfit functional (19) when solving the MICP. Once the PGD solution is available, the value of the functional $\mathcal{J}$ as a function of the conductivities is readily computed. This enables the use of nonlinear constrained optimization algorithms, not necessarily developed for differential problems. Specifically, we tested our method with a generic solver like the sequential quadratic programming (SQP) method [74], implemented by the `fmincon` routine in MATLAB®. The possibility of using this kind of solvers is clearly a practical advantage of the *online* phase.

We present the results about the conductivity evaluation in a synthetic setting, where the data used as observations are generated on a spatial discretization more refined in comparison with the one used for the model reduction. At each time step, we also add a Gaussian noise with zero mean and standard deviation equal to $p \max_{\mathbf{x},t} |u|$, where p is the noise-to-signal ratio. Synthetic measurements were recorded every $dt_{snap} = 2$ ms for a global duration of $T = 30$ ms, so that 15 voltage recordings are used to calculate $\mathcal{J}$. The observation domain, Ω_{obs}, consists of 8000 points equally distributed in the domain, which is comparable with the number of observation points characterizing standard optical mapping recordings [72]. The search is constrained to the admissible parametric space $\mathcal{S} = \mathcal{S}_l \times \mathcal{S}_t$ with $\mathcal{S}_l = [0.06, 0.09]\,\mathrm{cm}^2/\mathrm{ms}$, $\mathcal{S}_t = [0.01, 0.04]\,\mathrm{cm}^2/\mathrm{ms}$ ($\Delta_l = \Delta_t = 0.03$ cm^2/ms). We set $\boldsymbol{\sigma}_0 = (0.06, 0.025)$ cm^2/ms as initial guess. We evaluate the performance of the PGD method to solve the MICP varying the tolerance tol_e and the anisotropic ratio, $R_a = 2, 4, 6$ corresponding to $\boldsymbol{\sigma} = (0.07, 0.035)$ cm^2/ms, $\boldsymbol{\sigma} = (0.08, 0.02)$ cm^2/ms and $\boldsymbol{\sigma} = (0.084, 0.014)$ cm^2/ms, respectively. The computational cost for solving the MICP with PGD is negligible and cannot be directly compared with the variational technique used in [24, 25], as PGD takes advantage of the offline phase. However, we will demonstrate that the PGD-based solution of the MICP is advantageous even when including offline costs.

5.1. A 2D Canine Tissue Geometry

Considering the 2D canine mesh used in Section 4.3, we expect to get a more precise estimation for $R_a = 4$ since the PGD approximation showed to be more accurate than for the other choices of the conductivity pairs (see Fig. 2(c)).

The reliability of the estimation is assessed by looking specifically at the value of σ_t since it controls the CVs. Table 7 gathers the results varying tol_e, the anisotropy ratio and p. Regardless of the tolerance selected and the value of p, the best estimates are obtained for $\boldsymbol{\sigma}_{exact} = (0.08, 0.02)$ cm^2/ms, the PGD approximation being in such a case closer to the FE solution. The recovery of the parameter σ_t is particularly precise and exhibits a low sensitivity to p, meaning that we can reconstruct the true propagation dynamics with a reliable prediction for the CVs. On the contrary, more variability affects σ_l estimates. This is in accordance

with the results in Section 4.3, where we noticed that the PGD solution depends more on the parameter σ_t, which controls the CVs, while it is less sensitive to the value of σ_l. As for the other conductivity pairs, the estimation obtained with tol_e=10^{-4} is less precise, especially for the high CV case, $R_a = 2$, consistently with the fact that the PGD error is higher in this case, as shown in Fig. 2(c). An overall improvement of the results is evident for lower tolerance values. For tol_e=10^{-6}, the estimates are accurate and robust with respect to the presence of noise in the data.

In view of a better estimation in the case of high CVs, we restrict the admissible range for σ_t, by choosing a length $\Delta_t = 0.01$ and 0.02 cm^2/ms, respectively. The same strategy has been used in Section 4.3 to reduce the error of the PGD approximation (see Fig. 5). Table 8 shows a more precise estimation when using $\Delta_t = 0.01$ cm^2/ms both for tol_e=10^{-4} and 10^{-5}. This agrees with the results in Fig. 5 where, for $\Delta_t = 0.01$ cm^2/ms, the PGD method is able to capture fast propagating excitable waves. Regarding $\Delta_t = 0.02$ cm^2/ms, an improvement is visible only for tol_e=10^{-5}. Results are robust with respect to the percentage, p, of noise.

The extremely fast evaluation of the reduced solution in the PGD online phase makes inversion remarkably inexpensive. In fact, solving the MICP using the PGD approximation of the transmembrane potential requires, at most, only 30 s (see Table 9).

The results presented so far suggest some practical ideas on using the PGD for solving the MICP, even with $\text{tol}_e = 10^{-4}$. In a sort of Predictor-Corrector approach, the PGD with a large tolerance can be used to inform a second-level computation. The latter can be performed either with PGD again but with a much narrowed exploration interval for the parameters (as suggested by strategy (c) in the previous Section) or with a fill-order solution, i.e. using the classical FE solver. The latter idea was used here in the case of $\boldsymbol{\sigma}_{exact} = (0.07, 0.035)$ cm^2/ms and tol_e=10^{-4}. Solving the MICP with a FE approximation and starting from the PGD estimate $\boldsymbol{\sigma}_0 = (0.0657, 0.0328)$ cm^2/ms takes 527 s to reach convergence with the final estimation $\boldsymbol{\sigma} = (0.07, 0.0349)$ cm^2/ms, to compare with 3293 s needed starting from $\boldsymbol{\sigma}_0 = (0.06, 0.025)$ cm^2/ms to reach a similar estimate, precisely, $\boldsymbol{\sigma} = (0.0702, 0.0360)$ cm^2/ms.

5.2. A 3D Canine Tissue Geometry

The MICP with PGD technique has been tested with the 3D canine geometry in Section 4.3. The case tol_e=10^{-6} has not been considered because the offline phase would be too expensive. As the PGD approximation for the propagation of the transmembrane potential in 3D yields results similar to the 2D case (see Section 4.3), we do expect results qualitatively comparable to the ones obtained in the 2D framework also for the MICP-PGD procedure. This is confirmed in Table 10. We obtain better results for $\boldsymbol{\sigma}_{exact} = (0.08, 0.02)$ cm^2/ms with high precision for the parameter σ_t and a general improvement of the estimation when decreasing the tolerance value to 10^{-5}. We highlight also for this test case the huge computational saving provided by the combination of MICP with PGD. In fact, despite the large number of DOFs of the

$p = 1\%, [\boldsymbol{\sigma}] = \text{mm}^2/\text{ms}$

	$R_a = 2$ $\boldsymbol{\sigma}_{exact}$ =(7.00, 3.50)	$R_a = 4$ $\boldsymbol{\sigma}_{exact}$ =(8.00, 2.00)	$R_a = 6$ $\boldsymbol{\sigma}_{exact}$ =(8.40, 1.40)
tol_e=10^{-4}	(6.57,3.28)	(8.11,1.93)	(8.98,1.29)
tol_e=10^{-5}	(6.93,3.96)	(7.71,1.96)	(8.57,1.34)
tol_e=10^{-6}	(6.90,3.56)	(7.80,1.96)	(8.22,1.35)

$p = 5\%, [\boldsymbol{\sigma}] = \text{mm}^2/\text{ms}$

	$R_a = 2$ $\boldsymbol{\sigma}_{exact} = (7.00, 3.50)$	$R_a = 4$ $\boldsymbol{\sigma}_{exact} = (8.00, 2.00)$	$R_a = 6$ $\boldsymbol{\sigma}_{exact} = (8.40, 1.40)$
tol_e=10^{-4}	(6.56,3.27)	(7.91,1.93)	(8.97,1.31)
tol_e=10^{-5}	(6.95,3.96)	(7.76,1.95)	(8.78,1.35)
tol_e=10^{-6}	(6.83,3.56)	(7.84,1.97)	(8.31,1.35)

$p = 10\%, [\boldsymbol{\sigma}] = \text{mm}^2/\text{ms}$

	$R_a = 2$ $\boldsymbol{\sigma}_{exact} = (7.00, 3.50)$	$R_a = 4$ $\boldsymbol{\sigma}_{exact} = (8.00, 2.00)$	$R_a = 6$ $\boldsymbol{\sigma}_{exact} = (8.40, 1.40)$
tol_e=10^{-4}	(6.55,3.24)	(8.05,1.93)	(8.98,1.30)
tol_e=10^{-5}	(6.96,3.97)	(7.73,1.95)	(8.44,1.36)
tol_e=10^{-6}	(6.82,3.56)	(7.91,1.96)	(8.26,1.35)

Table 7: 2D canine tissue: conductivity estimation provided by the PGD-MICP procedure varying the external tolerance, the anisotropy ratio and the percentage of noise. For the sake of readability, we display the conductivities in mm^2/ms.

$\text{tol}_e = 10^{-4}, [\boldsymbol{\sigma}] = \text{mm}^2/\text{ms}$

	$p = 1\%$	$p = 5\%$	$p = 10\%$
Δ_t=0.03	(6.57,3.28)	(6.56,3.27)	(6.55,3.24)
Δ_t=0.02	(7.85,3.71)	(7.86,3.73)	(7.84,3.71)
Δ_t=0.01	(6.91,3.33)	(6.90,3.32)	(6.91,3.35)

$\text{tol}_e = 10^{-5}, [\boldsymbol{\sigma}] = \text{mm}^2/\text{ms}$

	$p = 1\%$	$p = 5\%$	$p = 10\%$
Δ_t=0.03	(6.93,3.96)	(6.95,3.96)	(6.96,3.97)
Δ_t=0.02	(6.40,3.66)	(6.39,3.66)	(6.40,3.65)
Δ_t=0.01	(6.80,3.35)	(6.75,3.35)	(6.82,3.34)

Table 8: 2D canine tissue: estimation of the conductivity $\boldsymbol{\sigma}_{exact} = (0.07, 0.035)$ provided by the MICP-PGD procedure varying the external tolerance, the length of the admissible domain Δ_t for σ_t and the percentage of noise. For the sake of readability, we display the conductivities in mm^2/ms.

	2D canine tissue	3D canine tissue	Real ventricle
tol_e=10^{-4}	22	154	32
tol_e=10^{-5}	25	180	36
tol_e=10^{-6}	30	/	40

Table 9: Execution time [s] associated with the MICP-PGD approach varying the external tolerance. The times are average values since they may vary depending on the realization of the noise random variable and on the initial guess of the optimization procedure.

3D mesh (roughly 135K), the solution of the inverse problem only requires about 180 s when $\text{tol}_e = 10^{-5}$, as highlighted in Table 9.

$p = 1\%, [\boldsymbol{\sigma}] = \text{mm}^2/\text{ms}$

	$R_a = 2$ $\boldsymbol{\sigma}_{exact} = (7.00, 3.50)$	$R_a = 4$ $\boldsymbol{\sigma}_{exact} = (8.00, 2.00)$	$R_a = 6$ $\boldsymbol{\sigma}_{exact} = (8.40, 1.40)$
tol_e=10^{-4}	(6.78,3.21)	(8.07,1.98)	(8.98,1.32)
tol_e=10^{-5}	(6.97,3.98)	(7.82,1.99)	(8.38,1.37)

$p = 5\%, [\boldsymbol{\sigma}] = \text{mm}^2/\text{ms}$

	$R_a = 2$ $\boldsymbol{\sigma}_{exact} = (7.00, 3.50)$	$R_a = 4$ $\boldsymbol{\sigma}_{exact} = (8.00, 2.00)$	$R_a = 6$ $\boldsymbol{\sigma}_{exact} = (8.40, 1.40)$
tol_e=10^{-4}	(6.90,3.20)	(8.11,1.97)	(8.96,1.31)
tol_e=10^{-5}	(6.98,4.00)	(8.56,1.99)	(8.38,1.39)

$p = 10\%, [\boldsymbol{\sigma}] = \text{mm}^2/\text{ms}$

	$R_a = 2$ $\boldsymbol{\sigma}_{exact} = (7.00, 3.50)$	$R_a = 4$ $\boldsymbol{\sigma}_{exact} = (8.00, 2.00)$	$R_a = 6$ $\boldsymbol{\sigma}_{exact} = (8.40, 1.40)$
tol_e=10^{-4}	(6.81,3.25)	(8.13,1.96)	(9.00,1.32)
tol_e=10^{-5}	(6.97,4.00)	(7.92,1.99)	(8.45,1.39)

Table 10: 3D canine tissue: conductivity estimation provided by the PGD-MICP procedure varying the external tolerance, the anisotropy ratio and the percentage of noise. For the sake of readability, we display the conductivities in mm^2/ms.

5.3. A Real Ventricle

Finally, we analyze the estimation obtained in the real left ventricular test case. As previously discussed, the PGD approximation applied to this geometry is more sensitive to the anisotropy ratio, R_a, and features higher errors (see Fig. 9). Therefore, the precision of the inversion may be affected. From Table 11, we note that using the PGD basis obtained with tol_e=10^{-4} leads to acceptable results only for $\boldsymbol{\sigma}_{exact} = (0.07, 0.035)$ cm^2/ms, whereas in the other tests the estimates it is fairly inaccurate, especially for σ_l. The estimates become more accurate as the tolerance decreases and reasonably match the exact conductivities in the case $\boldsymbol{\sigma}_{exact} = (0.07, 0.035)$ cm^2/ms and $\boldsymbol{\sigma}_{exact} = (0.08, 0.02)$ cm^2/ms, whereas the estimation of σ_l for $\boldsymbol{\sigma}_{exact} = (0.084, 0.014)$ cm^2/ms still lacks accuracy even for tol_e=10^{-6}. This agrees with the error pattern shown in Fig. 9, where, for these particular parameter values, the discrepancy between FE and PGD solutions increases when reducing the tolerance. A possible strategy, in this case, is to refine the space discretization for the PGD solver. Table 9 confirms the computational advantages led by solving the MICP with PGD, estimations being obtained in, at most ,40 s.

6. Conclusions and Perspectives

The patient-specific customization of mathematical models is a crucial step to bring numerical modeling into the clinical routine. Unfortunately, the high computational costs of standard data assimilation procedures conflict with clinical time frames. Ideally, one would like to have a nearly real-time estimate of the

$p = 1\%, [\boldsymbol{\sigma}] = \text{mm}^2/\text{ms}$

	$R_a = 2$ $\boldsymbol{\sigma}_{exact} = (7.00, 3.50)$	$R_a = 4$ $\boldsymbol{\sigma}_{exact} = (8.00, 2.00)$	$R_a = 6$ $\boldsymbol{\sigma}_{exact} = (8.40, 1.40)$
tol_e=10^{-4}	(6.53,3.46)	(8.98,1.56)	(7.10,1.22)
tol_e=10^{-5}	(6.79,3.77)	(7.40,1.88)	(7.40,1.31)
tol_e=10^{-6}	(6.75,3.62)	(7.57,2.06)	(7.70,1.45)

$p = 5\%, [\boldsymbol{\sigma}] = \text{mm}^2/\text{ms}$

	$R_a = 2$ $\boldsymbol{\sigma}_{exact} = (7.00, 3.50)$	$R_a = 4$ $\boldsymbol{\sigma}_{exact} = (8.00, 2.00)$	$R_a = 6$ $\boldsymbol{\sigma}_{exact} = (8.40, 1.40)$
tol_e=10^{-4}	(6.54,3.45)	(9.00,1.57)	(7.20,1.21)
tol_e=10^{-5}	(6.81,3.78)	(7.36,1.88)	(7.46,1.20)
tol_e=10^{-6}	(6.78,3.62)	(7.56,2.06)	(7.71,1.43)

$p = 10\%, [\boldsymbol{\sigma}] = \text{mm}^2/\text{ms}$

	$R_a = 2$ $\boldsymbol{\sigma}_{exact} = (7.00, 3.50)$	$R_a = 4$ $\boldsymbol{\sigma}_{exact} = (8.00, 2.00)$	$R_a = 6$ $\boldsymbol{\sigma}_{exact} = (8.40, 1.40)$
tol_e=10^{-4}	(6.55,3.45)	(8.90,1.56)	(7.21,1.21)
tol_e=10^{-5}	(6.80,3.77)	(7.31,1.94)	(7.41,1.27)
tol_e=10^{-6}	(6.79,3.60)	(7.58,2.06)	(7.69,1.46)

Table 11: Real ventricle: conductivity estimation provided by the PGD-MICP procedure varying the external tolerance, the anisotropy ratio and the percentage of noise. For the sake of readability, we display the conductivities in mm^2/ms.

patient-specific parameters. Specific model reduction methods that may retain the clinical accuracy of the full mode (i.e., the accuracy needed for diagnosing or decision-making), with a significant improvement of the computational efficiency are crucial, for instance, in uncertainty quantification and parameter estimation (see, e.g., [75, 76, 77, 78, 79]).

In the specific field of electrophysiology, the need of an accurate estimation of the conductivities in the Monodomain problem is associated with many possible applications, for instance when dealing with the optimal placement of a pace-maker or the identification of ablation sites [80, 81, 82, 83, 84]. Parameter estimation calls for accurate and efficient model reduction techniques. However, consolidated model reduction techniques, like the POD, may suffer from a non optimal selection of the snapshots. In this paper, a snapshot-free model order reduction technique like PGD, thus circumventing one of the main drawbacks of POD. In spite of a significant offline cost, the minimal cost of the online phase makes PGD very competitive with respect to other model reduction techniques, in particular, when involved in multi-query contexts, such as the resolution of inverse problems.

What presented here is just a preliminary step of a more complex series of possible developments. Among these: (1) the extension to more complex ionic models (and, eventually, to the Bidomain model) is not trivial, as the modeling of the ionic terms requires a specific factorization of the increased linear functional $\mathcal{F}$; (2) the rapid solution of the online phase makes affordable the introduction of Uncertainty Quantification techniques, like the Bayesian ones. This is a critical step for the self-assessment of the quality of the parameter estimation;

(3) the cost of the offline phase could be dumped if recyclable on different geometries. This calls for the construction of a PGD library of offline solutions on a reference geometry to be successively mapped onto a real patient-specific morphology. While this approach might slow down the online phase, the overall benefit for a large pool of patients and, eventually, for clinical applications could be potentially high. Finally, there is the need of a deep theoretical analysis of the convergence of the iterative solvers of the PGD, to identify rigorously the conditions that guarantee the reliability of the approach and, possibly, appropriate acceleration techniques.

Encouraged by the extremely positive results reached in this work, we plan to pursue these developments in the next future.

Acknowledgements

AB and AV acknowledge the support of the NSF Project DMS 1412963 and the XSEDE Consortium, Grant TG-ASC160069. MGC wants to thank the Department of Mathematics at Emory University for hosting him during part of the research and the support of the Politecnico di Milano for the travel expenses. SP acknowledges the INdAM-GNCS Project 2019 *Advanced intrusive and non-intrusive model order reduction techniques and applications*. AG acknowledges the support of the Italian National Group for Mathematical Physics (GNFM-INdAM) Project *Constitutive modeling of active fiber-distributed media*.

References

[1] R. L. Winslow, N. Trayanova, D. Geman, M. I. Miller, Computational medicine: translating models to clinical care, Science translational medicine 4 (158) (2012) 158rv11–158rv11.

[2] L. Bertagna, M. D'Elia, M. Perego, A. Veneziani, Data assimilation in cardiovascular fluid–structure interaction problems: an introduction, in: Fluid-Structure Interaction and Biomedical Applications, Springer, 2014, pp. 395–481.

[3] C. Bertoglio, P. Moireau, J.-F. Gerbeau, Sequential parameter estimation for fluid–structure problems: Application to hemodynamics, International Journal for Numerical Methods in Biomedical Engineering 28 (4) (2012) 434–455.

[4] M. D'Elia, L. Mirabella, T. Passerini, M. Perego, M. Piccinelli, C. Vergara, A. Veneziani, Applications of variational data assimilation in computational hemodynamics, in: Modeling of Physiological Flows, Springer, 2012, pp. 363–394.

[5] A. Veneziani, C. Vergara, Inverse problems in cardiovascular mathematics: toward patient-specific data assimilation and optimization, International Journal for Numerical Methods in Biomedical Engineering 29 (7) (2013) 723–725.

[6] K. Law, A. Stuart, K. Zygalakis, Data assimilation, Cham, Switzerland: Springer.

[7] M. Asch, M. Bocquet, M. Nodet, Data assimilation: methods, algorithms, and applications, Vol. 11, SIAM, 2016.

[8] D. Amsallem, M. J. Zahr, C. Farhat, Nonlinear model order reduction based on local reduced-order bases, International Journal for Numerical Methods in Engineering 92 (10) (2012) 891–916.

[9] J. S. Hesthaven, G. Rozza, B. Stamm, Certified reduced basis methods for parametrized partial differential equations, Springer, 2016.

[10] A. Quarteroni, A. Manzoni, F. Negri, Reduced basis methods for partial differential equations: an introduction, Vol. 92, Springer, 2015.

[11] G. Rozza, D. B. P. Huynh, A. T. Patera, Reduced basis approximation and a posteriori error estimation for affinely parametrized elliptic coercive partial differential equations, Archives of Computational Methods in Engineering 15 (3) (2007) 1.

[12] Z. Luo, G. Chen, Proper orthogonal decomposition methods for partial differential equations, Academic Press, 2018.

[13] F. S. Costabal, P. Perdikaris, E. Kuhl, D. E. Hurtado, Multi-fidelity classification using gaussian processes: Accelerating the prediction of large-scale computational models, Computer Methods in Applied Mechanics and Engineering 357 (2019) 112602.

[14] R. H. Clayton, O. Bernus, E. M. Cherry, H. Dierckx, F. H. Fenton, L. Mirabella, A. V. Panfilov, F. B. Sachse, G. Seemann, H. Zhang, Models of cardiac tissue electrophysiology: progress, challenges and open questions, Progress in biophysics and molecular biology 104 (1-3) (2011) 22–48.

[15] L. Glass, P. Hunter, A. McCulloch, Theory of heart: biomechanics, biophysics, and nonlinear dynamics of cardiac function, Springer Science & Business Media, 2012.

[16] A. J. Pullan, L. K. Cheng, M. L. Buist, Mathematically modelling the electrical activity of the heart: from cell to body surface and back again, World scientific, 2005.

[17] F. Fenton, E. Cherry, Models of cardiac cell, Scholarpedia 3 (8) (2008) 1868.

[18] P. Lenarda, A. Gizzi, M. Paggi, A modeling framework for electro-mechanical interaction between excitable deformable cells, European Journal of Mechanics-A/Solids 72 (2018) 374–392.

[19] S. Weinberg, Ephaptic coupling rescues conduction failure in weakly coupled cardiac tissue with voltage-gated gap junctions, Chaos 27 (9) (2017) 093908.

[20] A. Loppini, A. Gizzi, C. Cherubini, E. Cherry, F. Fenton, S. Filippi, Spatiotemporal correlation uncovers characteristic lengths in cardiac tissue, Physical Review E 100 (2) (2019) 020201.

[21] L. S. Graham, D. Kilpatrick, Estimation of the bidomain conductivity parameters of cardiac tissue from extracellular potential distributions initiated by point stimulation, Annals of biomedical engineering 38 (12) (2010) 3630–3648.

[22] Y. Abidi, M. Mahjoub, N. Zemzemi, Ionic parameters estimation in multi-scale cardiac electrophysiology modelling, Tech. rep., INRIA, Bordeaux, FR (2019).

[23] H. Yang, A. Veneziani, Estimation of cardiac conductivities in ventricular tissue by a variational approach, Inverse Problems 31 (11) (2015) 115001.

[24] A. Barone, F. Fenton, A. Veneziani, Numerical sensitivity analysis of a variational data assimilation procedure for cardiac conductivities, Chaos: An Interdisciplinary Journal of Nonlinear Science 27 (2017) 093930.

[25] A. Barone, A. Gizzi, F. Fenton, S. Filippi, A. Veneziani, Experimental validation of a variational data assimilation procedure for estimating space-dependent cardiac conductivities, Computer Methods in Applied Mechanics and Engineering 358.

[26] M. Boulakia, E. Schenone, J.-F. Gerbeau, Reduced-order modeling for cardiac electrophysiology. application to parameter identification, International Journal for Numerical Methods in Biomedical Engineering 28 (6-7) (2012) 727–744.

[27] J.-F. Gerbeau, D. Lombardi, E. Schenone, Reduced order model in cardiac electrophysiology with approximated lax pairs, Advances in Computational Mathematics 41 (5) (2015) 1103–1130.

[28] S. Pagani, A. Manzoni, A. Quarteroni, Numerical approximation of parametrized problems in cardiac electrophysiology by a local reduced basis method, Computer Methods in Applied Mechanics and Engineering 340 (2018) 530–558.

[29] H. Yang, A. Veneziani, Efficient estimation of cardiac conductivities via pod-deim model order reduction, Applied Numerical Mathematics 115 (2017) 180–199.

[30] F. Chinesta, R. Keunings, A. Leygue, The Proper Generalized Decomposition for Advanced Numerical Simulations: a Primer, SpringerBriefs in Applied Sciences and Technology, Springer International Publishing, 2014.

[31] A. Ammar, E. Cueto, F. Chinesta, Reduction of the chemical master equation for gene regulatory networks using proper generalized decompositions, International Journal for Numerical Methods in Biomedical Engineering 28 (9) (2012) 960–973.

[32] S. Niroomandi, D. González, I. Alfaro, F. Bordeu, A. Leygue, E. Cueto, F. Chinesta, Real-time simulation of biological soft tissues: a PGD approach, International Journal for Numerical Methods in Biomedical Engineering 29 (5) (2013) 586–600.

[33] M. Signorini, S. Zlotnik, P. Díez, Proper generalized decomposition solution of the parameterized Helmholtz problem: application to inverse geophysical problems, International Journal for Numerical Methods in Engineering 109 (8) (2017) 1085–1102.

[34] P. Ladevèze, J.-C. Passieux, D. Néron, The LATIN multiscale computational method and the proper generalized decomposition, Computer Methods in Applied Mechanics and Engineering 199 (21-22) (2010) 1287–1296.

[35] E. Pruliere, F. Chinesta, A. Ammar, On the deterministic solution of multidimensional parametric models using the proper generalized decomposition, Mathematics and Computers in Simulation 81 (4) (2010) 791–810.

[36] J. Lions, E. Magenes, Non Homogeneous Boundary Value Problems and Applications, Springer, Berlin, 1972.

[37] Y. Pinchover, J. Rubinstein, An Introduction to Partial Differential Equations, Cambridge University Press, Cambridge, 2005.

[38] S. Perotto, M. G. Carlino, F. Ballarin, Model reduction by separation of variables: a comparison between hierarchical model reduction and proper generalized decomposition, in: S. Sherwin, D. Moxey, C. Schwab, J. Peiro, P. E. Vincent (Eds.), Spectral and High Order Methods for Partial Differential Equations ICOSAHOM 2018, Springer, 2020.

[39] A. L. Hodgkin, A. F. Huxley, A quantitative description of membrane current and its application to conduction and excitation in nerve, The Journal of physiology 117 (4) (1952) 500–544.

[40] J. Keener, J. Sneyd, Mathematical Physiology, Spinger–Verlag, 2009.

[41] J. Sundnes, G. T. Lines, X. Cai, B. F. Nielsen, K.-A. Mardal, A. Tveito, Computing the electrical activity in the heart, Vol. 1, Springer Science & Business Media, 2007.

[42] S. Luther, F. H. Fenton, B. Kornreich, A. Squires, P. Bittihn, D. Hornung, M. Zabel, J. Flanders, A. Gladuli, L. Campoy, E. Cherry, Low-energy control of electrical turbulence in the heart, Nature 475 (2011) 235–239.

[43] P. Colli Franzone, L. F. Pavarino, A parallel solver for reaction–diffusion systems in computational electrocardiology, Mathematical models and methods in applied sciences 14 (06) (2004) 883–911.

[44] L. Gerardo-Giorda, L. Mirabella, F. Nobile, M. Perego, A. Veneziani, A model-based block-triangular preconditioner for the bidomain system in electrocardiology, Journal of Computational Physics 228 (10) (2009) 3625–3639.

[45] L. Gerardo-Giorda, M. Perego, A. Veneziani, Optimized schwarz coupling of bidomain and monodomain models in electrocardiology, ESAIM: Mathematical Modelling and Numerical Analysis 45 (2) (2011) 309–334.

[46] S. Linge, J. Sundnes, M. Hanslien, G. T. Lines, A. Tveito, Numerical solution of the bidomain equations, Philosophical Transactions of the Royal Society A: Mathematical, Physical and Engineering Sciences 367 (1895) (2009) 1931–1950.

[47] L. Mirabella, F. Nobile, A. Veneziani, An a posteriori error estimator for model adaptivity in electrocardiology, Computer Methods in Applied Mechanics and Engineering 200 (37-40) (2011) 2727–2737.

[48] L. F. Pavarino, S. Scacchi, Multilevel additive schwarz preconditioners for the bidomain reaction-diffusion system, SIAM Journal on Scientific Computing 31 (1) (2008) 420–443.

[49] L. F. Pavarino, S. Scacchi, Parallel multilevel schwarz and block preconditioners for the bidomain parabolic-parabolic and parabolic-elliptic formulations, SIAM Journal on Scientific Computing 33 (4) (2011) 1897–1919.

[50] M. Perego, A. Veneziani, An efficient generalization of the rush-larsen method for solving electrophysiology membrane equations, Electronic Transactions on Numerical Analysis 35 (2009) 234–256.

[51] G. Plank, M. Liebmann, R. W. dos Santos, E. J. Vigmond, G. Haase, Algebraic multigrid preconditioner for the cardiac bidomain model, IEEE transactions on bio-medical engineering 54 (4) (2007) 585.

[52] E. J. Vigmond, F. Aguel, N. A. Trayanova, Computational techniques for solving the bidomain equations in three dimensions, IEEE Transactions on Biomedical Engineering 49 (11) (2002) 1260–1269.

[53] E. J. Vigmond, R. W. Dos Santos, A. J. Prassl, M. Deo, G. Plank, Solvers for the cardiac bidomain equations, Progress in biophysics and molecular biology 96 (1-3) (2008) 3–18.

[54] D. E. Hurtado, G. Rojas, Non-conforming finite-element formulation for cardiac electrophysiology: an effective approach to reduce the computation time of heart simulations without compromising accuracy, Computational Mechanics 61 (4) (2018) 485–497.

[55] C. Luo, Y. Rudy, A model of the ventricular cardiac action potential. depolarization, repolarization, and their interaction., Circulation research 68 (6) (1991) 1501–1526.

[56] C. Luo, Y. Rudy, A dynamic model of the cardiac ventricular action potential. i. simulations of ionic currents and concentration changes., Circulation research 74 (6) (1994) 1071–1096.

[57] K. H. W. J. Ten Tusscher, D. Noble, P.-J. Noble, A. V. Panfilov, A model for human ventricular tissue, American Journal of Physiology-Heart and Circulatory Physiology 286 (4) (2004) H1573–H1589.

[58] E. M. Cherry, F. H. Fenton, Effects of boundaries and geometry on the spatial distribution of action potential duration in cardiac tissue, Journal of Theoretical Biology 285 (2011) 164–176.

[59] G. A. Holzapfel, R. W. Ogden, Constitutive modelling of passive myocardium: a structurally based framework for material characterization, Philosophical Transactions of the Royal Society A: Mathematical, Physical and Engineering Sciences 367 (1902) (2009) 3445–3475.

[60] M. S. Spach, Anisotropy of cardiac tissue: a major determinant of conduction, Journal of cardiovascular electrophysiology 10 (6) (1999) 887–890.

[61] M. S. Spach, J. F. Heidlage, R. C. Barr, P. C. Dolber, Cell size and communication: role in structural and electrical development and remodeling of the heart, Heart Rhythm 1 (4) (2004) 500–515.

[62] L. Clerc, Directional differences of impulse spread in trabecular muscle from mammalian heart., The Journal of physiology 255 (2) (1976) 335–346.

[63] D. E. Roberts, L. T. Hersh, A. M. Scher, Influence of cardiac fiber orientation on wavefront voltage, conduction velocity, and tissue resistivity in the dog., Circulation research 44 (5) (1979) 701–712.

[64] D. E. Roberts, A. M. Scher, Effect of tissue anisotropy on extracellular potential fields in canine myocardium in situ., Circulation Research 50 (3) (1982) 342–351.

[65] P. R. Johnston, A sensitivity study of conductivity values in the passive bidomain equation, Mathematical biosciences 232 (2) (2011) 142–150.

[66] M. G. Carlino, Model reduction by proper generalized decomposition in electrocardiology, Master's thesis, Politecnico di Milano (2017).

[67] A. Ern, J.-L. Guermond, Theory and Practice of Finite Elements, Vol. 159 of Applied Mathematical Sciences, Springer-Verlag, New York, 2004.

[68] Y. Saad, Iterative methods for sparse linear systems, Vol. 82, siam, 2003.

[69] L. Bertagna, S. Deparis, L. Formaggia, D. Forti, A. Veneziani, The lifev library: engineering mathematics beyond the proof of concept, arXiv preprint arXiv:1710.06596.

[70] T. Passerini, A. Quaini, U. Villa, A. Veneziani, S. Canic, Validation of an open source framework for the simulation of blood flow in rigid and deformable vessels, International journal for numerical methods in biomedical engineering 29 (11) (2013) 1192–1213.

[71] M. Heroux, R. Bartlett, V. Hoekstra, J. Hu, T. Kolda, R. Lehoucq, K. Long, R. Pawlowski, E. Phipps, A. Salinger, H. Thornquist, An Overview of Trilinos, Tech. Rep. SAND2003-2927, Sandia National Laboratories (2003).

[72] A. Gizzi, E. M. Cherry, J. Gilmour, R. F., S. Luther, S. Filippi, F. H. Fenton, Effects of pacing site and stimulation history on alternans dynamics and the development of complex spatiotemporal patterns in cardiac tissue, Frontiers in Physiology 4 (2013) 1–20.

[73] F. Fenton, S. Luther, E. Cherry, N. Otani, V. Krinsky, A. Pumir, E. Bodenschatz, R. Gilmour Jr, Termination of atrial fibrillation using pulsed low-energy far-field stimulation, Circulation 120 (2009) 467.

[74] J. Nocedal, S. Wright, Numerical optimization, Springer Science & Business Media, 2006.

[75] Y. A. Brandes Costa Barbosa, Isogeometric hierarchical model reduction: from analysis to patient-specific simulations, Ph.D. thesis, Politecnico di Milano (2020).

[76] L. Mansilla Alvarez, P. Blanco, C. Bulant, E. Dari, A. Veneziani, R. Feijóo, Transversally enriched pipe element method (tepem): An effective numerical approach for blood flow modeling, International journal for numerical methods in biomedical engineering 33 (4) (2017) e2808.

[77] S. Guzzetti, L. M. Alvarez, P. Blanco, K. T. Carlberg, A. Veneziani, Propagating uncertainties in large-scale hemodynamics models via network uncertainty quantification and reduced-order modeling, Computer Methods in Applied Mechanics and Engineering 358 (2020) 112626.

[78] C. M. Fleeter, G. Geraci, D. E. Schiavazzi, A. M. Kahn, A. L. Marsden, Multilevel and multifidelity uncertainty quantification for cardiovascular hemodynamics (2019). arXiv:1908.04875.

[79] J. Seo, C. Fleeter, A. M. Kahn, A. L. Marsden, D. E. Schiavazzi, Multi-fidelity estimators for coronary circulation models under clinically-informed data uncertainty (2019). arXiv:1911.11266.

[80] K. Kunisch, M. Wagner, Optimal control of the bidomain system (i): The monodomain approximation with the rogers-mcculloch model, Nonlinear Analysis: Real World Applications 13 (4) (2012) 1525–1550.

[81] K. Kunisch, M. Wagner, Optimal control of the bidomain system (ii): Uniqueness and regularity theorems for weak solutions, Annali di Matematica Pura ed Applicata 192 (6) (2013) 951–986.

[82] K. Kunisch, M. Wagner, Optimal control of the bidomain system (iii): Existence of minimizers and first-order optimality conditions, ESAIM: Mathematical Modelling and Numerical Analysis 47 (4) (2013) 1077–1106.

[83] C. Nagaiah, K. Kunisch, G. Plank, Optimal control approach to termination of re-entry waves in cardiac electrophysiology, Journal of Mathematical Biology 67 (2) (2013) 359–388.

[84] A. Petras, M. Leoni, J. M. Guerra, J. Jansson, L. Gerardo-Giorda, Tissue drives lesion: computational evidence of interspecies variability in cardiac radiofrequency ablation, in: International Conference on Functional Imaging and Modeling of the Heart, Springer, 2019, pp. 139–146.

[85] C. C. Mitchell, D. G. Schaeffer, A two-current model for the dynamics of cardiac membrane, Bulletin of mathematical biology 65 (5) (2003) 767–793.

[86] F. Fenton, A. Karma, Vortex dynamics in three-dimensional continuous myocardium with fiber rotation: Filament instability and fibrillation, Chaos: An Interdisciplinary Journal of Nonlinear Science 8 (1) (1998) 20–47.

[87] A. Bueno-Orovio, E. M. Cherry, F. H. Fenton, Minimal model for human ventricular action potentials in tissue, Journal of theoretical biology 253 (3) (2008) 544–560.

Appendix A. PGD Approximation of the Whole Action Potential

The simulations considered in the body of this work only focused on the *wavefront* propagation to limit computational costs related to the offline phase. Here we investigate the accuracy of the PGD method to reconstruct the *waveback* propagation. For this purpose, we set T=150 ms to capture the whole Action

Potential (AP). We refer to the 2D canine tissue geometry with $\boldsymbol{\sigma} = (0.08, 0.02)$ cm^2/ms and tol$_e$=10^{-4}. Fig. A.11 (a) compares the FE and the PGD transmembrane potentials at the mesh nodes featuring the highest approximation error. Error is negligible in the resting phase (in this case, roughly in the interval [0,20] ms and after 120 ms), when $u = 0$ mV, and in the plateau phase ([22,115] ms), when the transmembrane potential is slowly decreasing. On the contrary, the PGD approximation is less accurate when the transmembrane potential sharply changes. In particular, the error is more significant in the interval [20,22] ms characterizing the wavefront propagation than in the interval [115,120] ms when waveback propagation occurs. This is confirmed by Fig. A.11 (b) representing the L^2-norm of the absolute error associated with the PGD approximation for the potential with respect to the FE solution.

Fig. A.12 qualitatively compares the FE and the PGD solutions on the whole domain, by considering the two time times, $t = 22$ ms and $t = 118$ ms, which exhibit the highest error in the wavefront and in the waveback propagation, respectively. The PGD approximation of the wavefront is less accurate than for the waveback, as highlighted in the right panels.

We argue that the loss of precision in reconstructing the waveback propagation is due to the abrupt drop of the transmembrane potential prescribed by the Rogers-McCulloch (RM) ionic model (see Fig. A.11 (a)). Extending the PGD technique to more complex phenomenological models, such as the Mitchell-Schaeffer [85], the Fenton-Karma [86] and the Minimal [87] ones, that provide a more accurate reproduction of the cardiac AP, may improve the quality of the waveback approximation. As expected, a larger simulation time results in a heavier computational demand during the offline stage. In fact, Algorithm 1 requires 12 hours as opposed to 0.9 hours for the shorter simulation with $T = 30.5$ ms (see Table 4).

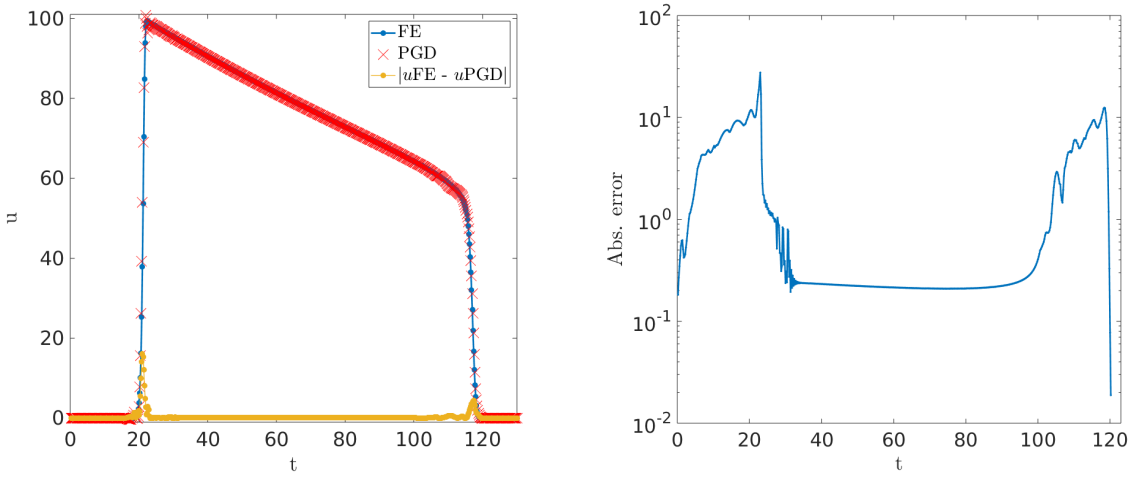

(a) (b)

Figure A.11: 2D canine tissue geometry: (a) comparison between the FE and the PGD solutions at the mesh nodes featuring the highest approximation error. (b) L^2-norm of the absolute error of the PGD approximation for the potential with respect to the FE solution, for $\boldsymbol{\sigma} = (0.08, 0.02)$ cm^2/ms and tol$_e$=10^{-4}.

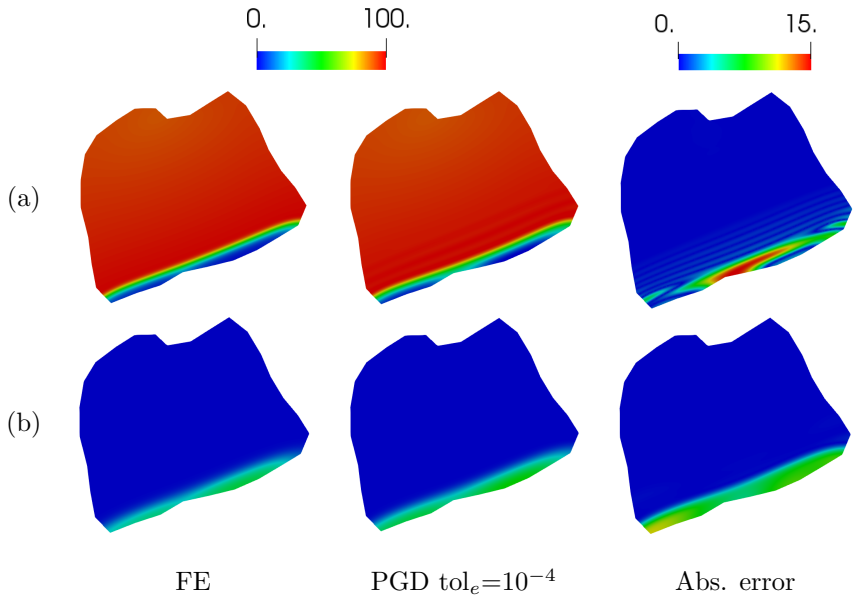

Figure A.12: 2D canine tissue geometry: comparison between the FE and the PGD approximations for the wavefront (a) and waveback (b) propagation [mV], and associated L^2-norm of the absolute error for $\boldsymbol{\sigma} = (0.08, 0.02)$ cm^2/ms and tol$_e$=10^{-4}.